

**Characterization and Modeling of Profiling Oceanographic Lidar for
Remotely Sampling Ocean Optical Properties**

by

Christopher Strait

A Thesis Submitted to the Faculty of

The Charles E. Schmidt College of Science

In Partial Fulfillment of the Requirements for the Degree of

Master of Science

Florida Atlantic University

Boca Raton, FL

December 2020

Copyright 2020 by Christopher Strait

Characterization and Modeling of Profiling Oceanic Lidar
For Remotely Sampling Ocean Optical Properties

by

Christopher M Strait

This thesis was prepared under the direction of the candidate's thesis advisor, Dr. Aditya Nayak, Department of Ocean and Mechanical Engineering, and has been approved by all members of the supervisory committee. It was submitted to the faculty of the Charles E. Schmidt College of Science and was accepted in partial fulfillment of the requirements for the degree of Master of Science.

SUPERVISORY COMMITTEE:



Aditya R Nayak (Dec 13, 2020 09:36 EST)

Aditya Nayak, Ph.D.

Thesis Advisor



Michael S Twardowski (Dec 13, 2020 17:09 EST)

Michael Twardowski, Ph.D.



Bing Ouyang (Dec 16, 2020 17:35 EST)

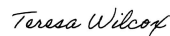
Bing Ouyang, Ph.D.



Peter McCarthy (Dec 16, 2020 17:37 EST)

Peter McCarthy, Ph.D.

Chair, Marine Science and Oceanography



Teresa Wilcox, Ph.D.

Interim Dean, Charles E. Schmidt College of
Science



Robert W. Stackman Jr. (Dec 17, 2020 08:38 EST)

Robert W. Stackman Jr., Ph.D.

Dean, Graduate College

December 17, 2020

Date

Acknowledgements

I would like to thank my committee members for all of their tenacity and help with this master thesis. This project would not have been possible without their input and help. I would also like to acknowledge Harbor Branch Oceanographic Institute for its focus on fostering student learning and expansion of our scientific understanding to better our natural environment. The facilities department at HBOI was extremely helpful in maintaining and aiding in tank preparations for experiments. I would also like to thank Brian Ramos and Ben Metzger for their help with both the workings and operation of the lidar and laser test range. I would also like to thank Fraser Dalgleish, without whom this project would have produced much less. While he ultimately was not an advisor on this project, his focus and drive to make this project successful cannot be overstated. My lab deserves a lot of credit for their input and patience during this process. I will always value their suggestions and conversations on how to maximize this project's potential.

Abstract:

Author: Christopher M. Strait
Title: Characterization and Modeling of Profiling Oceanographic Lidar for Remotely Sampling Ocean Optical Properties
Institution: Florida Atlantic University
Thesis Advisor: Aditya Nayak, PhD
Degree: Master of Science
Year: 2020

Lidar has the ability to supplant or compliment many current measurement technologies in ocean optics. Lidar measures Inherent Optical Properties over long distances without impacting the orientation and assemblages of particles it measures, unlike many systems today which require pumps and flow cells. As an active sensing technology, it has the benefit of being independent of time of day and weather. Techniques to interpret oceanographic lidar lags behind atmospheric lidar inversion techniques to measure optical properties due to the complexity and variability of the ocean. Unlike in the atmosphere, two unknowns in the lidar equation backscattering at 180° (β_π) and attenuation (c) do not necessarily covary. A lidar system developed at the Harbor Branch Oceanographic Institute is used as a test bed to validate a Monte-Carlo model to investigate the inversion of optical properties from lidar signals. Controlled tank experiments and field measurements are used to generate lidar waveforms and provide optical situations to model. The Metron EODES backscatter model is used to model waveforms. A chlorophyll based forward optical model provides a set of 1500 unique optical situations which are

modeled to test inversion techniques and lidar geometries. Due to issues with the lidar system and model the goal of validating the model as well as a more mature inversion experiment were not completed. However, the results are valuable to show the complexity and promise of lidar systems.

**Characterization and Modeling of Profiling Oceanographic Lidar for Remotely
Sampling Ocean Optical Properties**

List of Tables	x
List of Figures	xi
List of Equations	xv
1 Introduction	1
1.1 Optical Parameters: IOPs, AOPs and E.	2
1.2 Lidar: A short history	3
1.3 Lidar Basics and Components.....	6
1.3.1 PMT	7
1.3.2 Digitizers.....	7
1.3.3 Lasers	8
1.3.4 The Single Scatter Lidar Equation.....	10
1.4 Metron Backscatter Waveform Calculation.....	13
1.5 Lidar Backscatter Waveform Interpretation.....	15
2 Forward Modeling for Investigation into Inversion Approaches.	19
2.1 Introduction	19
2.2 Methods and Materials	20

2.2.1	Synthetic Dataset Creation.....	20
2.2.2	Geometric Model Inputs	23
2.2.3	Slope Calculation	24
2.2.4	Inversion Using Modified Gordon Methodology	24
2.3	Results	25
2.4	Conclusion.....	31
3	Characterization of Lidar Systems	33
3.1	Introduction	33
3.2	Methods and Materials	34
3.2.1	HBOI lidars.....	34
3.2.2	SN1 Field of View Characterization: a Baseline for Both Systems	38
3.2.3	Underwater Beam Divergence Measurement	38
3.2.4	Above Water Laser Divergence Measurement	39
3.2.5	SN2 Above Water Field of View Measurement	40
3.2.6	SN2 PMT Linearity.....	41
3.3	Results	41
3.3.1	SN1 Field of View Characterization.....	41
3.3.2	Underwater Beam Divergence Characterization	42
3.3.3	SN2 Above Water Field of View Measurement	43
3.3.4	Above Water Beam Characterization	45

3.3.5	SN2 PMT characterization.....	45
3.4	Conclusions	46
4	Tank, Model and Field Results of two Lidar System.	47
4.1	Introduction	47
4.2	Methods and Materials	47
4.2.1	Tank experiments.....	47
4.2.2	Lidar Measurement	49
4.2.3	SN1 Slope Calculation.....	49
4.2.4	Tank measurements	49
4.2.5	IOP Measurement	49
4.2.6	SN2 Field Data.....	50
4.2.7	SN2 Digitizer timing correction.....	51
4.2.8	SN2 Outlier Scan Removal.....	51
4.3	Results	52
4.3.1	SN1 Tank and Model Results	52
4.3.2	SN2 Lidar Tank, Model and Field Data.....	54
4.4	Conclusions	68
	Conclusion and future work.....	72
	Appendix.....	75
	References.....	77

List of Tables

Table 2.1: Geometry for Metron Model Runs in Half Angle.	24
Table 3.1: Green beam divergence results for both systems	45

List of Figures

Figure 1.1: General schematic of lidar system.....	6
Figure 1.2: Schematic showing lidar geometric arrangement in Metron backscatter model.	14
Figure 1.3: Example of a good waveform (i) and example of a malformed waveform (ii). Black lines are the waveform while the red lines are the linear regions over which the slope is calculated.	17
Figure 1.4: Gordon approximation from Monte-Carlo simulations of lidar attenuation coefficients normalized by the attenuation. Single scatter albedo showing for each calculation reported from Gordon (1982).	18
Figure 2.1: Schematic view of Metron backscattering module inputs.....	20
Figure 2.2: Fournier-Forand calculated phase functions derived from the backscattering ratio.	26
Figure 2.3: (i) Example waveforms with changing c for FOV 0.0175 rad, (ii) example waveforms with changing FOV at $c = 0.408 \text{ m}^{-1}$	28
Figure 2.4: Example plot between c and $\frac{K_{sys}}{c}$ for all [Chl] (black vertical lines) and for single scattering albedo (ω) binned by 0.0175 increments from 0.94 to 0.8.	29
Figure 2.5: Fit coefficients for all albedos and fields of view. i, ii and iii show fitted coefficients for the three degrees of freedom in the equation. iv shows the goodness of fit through the root mean square error.	30
Figure 2.6: Fit between field of view and geometry component of equation.	31

Figure 3.1: Side view of lidar system. Both SN1 and SN2 are identical, save for aperture and laser settings.	35
Figure 3.2: Source components showing both laser and beam combining optics.	36
Figure 3.3: Trigger optics for both lidar systems.....	37
Figure 3.4: Lidar telescope assemblies.	37
Figure 3.5: Setup for measuring beam divergence using Beamage 3.0 camera. X1 and X2 are the positions from the lidar which were measured.....	39
Figure 3.6: 3D in air field of View Setup.	40
Figure 3.7:Field of views for aperture values 10mm (blue), 5mm (Orange), 3mm (yellow) and 2mm (purple).....	41
Figure 3.8: Difference in apparent divergence given changes in shutter speed. The f stop was set to 1/16, the ISO was set to 10000 and the focal length was 40mm. The shutter speed was 1/8, 1/4, 1/2 and 4 seconds for i, ii, iii and iv respectively.....	42
Figure 3.9: Example plot of underwater field of view determination.....	43
Figure 3.10: Intensity profiles at reflector at 246.7 cm from the exit window.	44
Figure 4.1: Example BaSO ₄ measured (black) and simulated (red) matchchups for c 532 nm (i) 0.1 m ⁻¹ and (ii) 1 m ⁻¹	52
Figure 4.2: Relationship between measured attenuation with ac-9 and range corrected lidar slope, i.e., K_{sys} , of simulated waveforms at 532 nm for BaSO ₄	53
Figure 4.3: Ratio of the integral of the multiple scattering signal and the integral of the common volume.....	54
Figure 4.4: AZRD and Barium Sulfate addition numbers vs attenuation. Closed circles are AZRD and open circles are Barium Sulfate.....	55

Figure 4.5: Example of hard target return highlighting digitizer timing jitter.....	56
Figure 4.6: Average of scans before (black) and after (blue) timing correction, showing broadening of signal due to distance uncertainties.	57
Figure 4.7: Example enhancement at higher c scan (0.97 m^{-1}) showing enhancement after 4 meters.	58
Figure 4.8: Examples of Metron simulations and measured data fits for three attenuations 0.085 , 0.816 and 1.29 m^{-1} for i, ii and iii respectively.	60
Figure 4.9: c vs K_{sys} for measured tank data. Open circles and green line are BaSO_4 and closed circles with black line are AZRD.	61
Figure 4.10: c vs K_{sys} for simulated tank data. Open circles and green line are BaSO_4 and closed circles with black line are AZRD.	61
Figure 4.11: Comparison of K_{sys} calculated from both measured and simulated data for BaSO_4 and AZRD.	62
Figure 4.12: Map of Fort Lauderdale test track, the green and red lines are the tracks for 4/23/2019 and 4/24/2019 respectively.	63
Figure 4.13: Distribution of c values for Fort Lauderdale sampling sites. Only data where there is both lidar and IOPs are shown.	64
Figure 4.14: Example scans in deep water from 4/23/2019 at 11:01 with PMT at 475V. 65	
Figure 4.15: Example plot in deep water showing a scan from 4/23/19 at 10:59 with PMT at 475V.....	66
Figure 4.16: Example plot in shallow water showing a scan at 11:43 4/24/19 at PMT at 425V.....	67
Figure 4.17: c vs K_{sys} for averaged water column attenuations for field dataset.	67

Figure 4.18: Modified Gordon plot for Fort Lauderdale dataset.	68
---	----

List of Equations

(1.1).....	2
(1.2).....	2
(1.3).....	3
(1.4).....	11
(1.5).....	12
(1.6).....	17
(2.1).....	21
(2.2).....	22
(2.3).....	22
(2.4).....	22
(2.5).....	22
(2.6).....	22
(2.7).....	23
(2.8).....	25
(3.11).....	33
(3.2).....	39
(3.3).....	40
(4.1).....	50

1 Introduction

Using light to measure the properties of the ocean has fundamentally changed investigations into the large, temporally and spatially complex processes of the Earth. Remote sensing allows for a view of the surface of the ocean with unrivaled coverage. This data, however, provides a skin level view and does not probe the three-dimensional nature of the Earth's oceans. Furthermore, current optical platforms provide only a small column of information, while fundamentally altering their samples through pumping of the sample through flow cells. This perturbation fundamentally changes the particle assemblages and density differences which alter their optical signal.

Lidar (light detection and ranging), fundamentally is the measuring the backscattered return of discrete pulses of light as they propagate and scatter through a remote volume. By measuring the discrete pulses with accurate timing as they propagate, it is possible to measure the change in returned light due to the optical properties of the medium. Lidar has the distinct advantage of being able to measure large distances from a single platform. The distance the lidar can measure is based on the source power, and the capabilities of the receiver to appropriately account for the decrease in returned light as a function of distance without loss of sensitivity. Lidar also does not alter the natural particle assemblages when measuring unlike pumped systems. It is in this way that lidar is a natural successor to many profiling instrument platforms. With improvements in laser and receiver technologies, the size, weight and power (SWaP) of lidars are reduced significantly. It is

due to these properties that the marrying of lidar technology with underwater autonomous vehicles is a potent combination for measuring the optical properties of the ocean.

1.1 Optical Parameters: Inherent Optical Properties, Apparent Optical Properties and Irradiance

Optical measurement techniques dominate research utilizing both passive and active measurements. Most sensors used in laboratories are active, meaning that they provide their own light source and are not dependent on the geometry of the light field, i.e. spectrophotometers and fluorimeters. Passive technologies, such as satellite imaging, are dependent on the geometry of the light field. By linking the optical conditions of a water body to those constituents which alter the light field through absorption and scattering, it is possible to examine in detail many of the major conditions which control the physical, chemical and biological processes on Earth. Dominant optically significant constituents in the ocean include Chlorophyll-*a* concentration, suspended particles and dissolved humic and fluvic acids. Each of these regulates the underwater light field, and these constituents can be quantified by understanding the properties of the light field.

Inherent Optical Properties (IOPs) are those properties that are independent of the geometry of the light field, i.e. they are not affected by the distribution of incoming light. Measuring IOPs gives way to understanding the interaction between optically significant constituents with the light field on a fundamental level. The main IOPs are absorption (*a*), scattering (*b*) and their sum attenuation (*c*):

$$a + b = c \quad (1-1)$$

Absorption and scattering both can be broken into several constituent components:

$$a_t = a_{CDOM} + a_{ph} + a_{NAP} + a_w = a_g + a_p + a_w \quad (1-2)$$

$$b_t = b_p + b_w \quad (1-3)$$

Here the subscripts CDOM, *ph*, *NAP* and *w* represent the dissolved, organic particulate, non-algal particulate and water components respectively. The subscript *p* is total particulate or the sum of the organic and inorganic particle fractions. The single scatter albedo (ω_o) is the ratio of scattering to attenuation. The volume scattering function (VSF; β ($m^{-1}sr^{-1}$)) defines the angular distribution of scattering, and is typically normalized to *b* in order to generate phase functions ($\tilde{\beta}$ (sr^{-1})). Phase functions for particles or water can be generated and stored to allow calculation with any measured *b*.

Irradiance (*E*) is the radiant flux per unit area of a surface and has the units $\frac{W}{m^2}$. A common apparent optical property (AOP) which describes the distribution of *E* with depth is downwelling extinction coefficient (k_d). The downwelling extinction coefficient is the rate of loss of *E* per unit depth in the water column. The downwelling extinction coefficient is the rate of loss of *E* per unit depth in the water column.

1.2 Lidar: A short history

Lidar as a measurement technique has its genesis even before the invention of the laser in 1960 (Maiman 1960). Before World War II, investigations into methods to probe the upper atmosphere using optical measurements were explored. In the 1930s, attempts to measure air density profiles were conducted by measuring changes in scattering using searchlight beams. The height of the different scattering measurements was determined by scanning the receiving optics over the continuous beams, thus providing a geometric solution for height. Discrete pulses of light were used for the first time in 1938 to determine cloud base heights (Houston and Carswell 1978). The term lidar was coined in a meteorological journal in 1953 (Middleton and Spilhaus 1953). By 1969 it was reported

that over 20 lasers had been adopted by American meteorologists and were used on a routine basis for multiple applications (Fletcher 1969).

Lidar started a period of rapid expansion in the 1960s due to the invention of the laser. By the early 1970s, all basic lidar techniques had been suggested and demonstrated and in 1976 the first textbook on lidar was published. Further advancement in lidar has followed progress in optical and electronic technology. Lasers, digitizers and low light detection technologies have all improved significantly since the inception of the laser. Lasers have seen increases in the number of available wavelengths, greater stability, pulse width, beam shape options and spectral purity. The receiving optics also have improved by providing better optical filters with high transmissivity, narrow bandwidth, steep spectral slopes and data acquisition systems which provide higher dynamic ranges, faster digitizing; generally, more powerful computing capabilities have all helped to push the boundaries of lidar research.

Lidar in the oceanographic sphere has a diverse set of applications, these all straddle the intersections of science, industry and defense. Fish surveys, phytoplankton layer research, bubble research, measuring optical properties, imaging, object detection, underwater inspection, induced fluorescence measurements, communications and surface roughness measurements are all common uses for lidar. The diversity of lidar systems applications ensures their continued and expanded use.

Oceanographic lidars are deployed on many platforms such as satellites, airplanes, AUVs, profiling packages and on ships. Satellite and airborne systems provide superior spatial and temporal coverage, while ship based and profiling lidars provide greater penetrating depths and vertical resolution. The majority of available profiling systems on

AUVs are used for imaging and point cloud mapping for inspection of machinery and wreckage. To examine the history of lidar used for the retrieval of optical properties requires a look at airborne and spaceborne lidar. Oceanic lidars for inversion of optical properties have lagged behind their atmospheric cousins due to the complexity of ocean color, and the loss of signal from absorption in water.

While there have been air and space-borne lidars which have been used to measure chlorophyll and CDOM (Kim 1973; Hoge, Swift, and Yungel 1995), work on inverting lidar for IOPs was not being investigated in earnest until the past few decades. In the 1980s many groups demonstrated lidars which were used to produce IOPs from aircraft, however their results were qualitative and highlighted the difficulty of teasing out the effect of IOPs from the measured signal. In the early to mid 2000's, Churnside developed a lidar for the National Oceanic and Atmospheric Administration to examine fish populations (Churnside 2001). The fish lidar was later used in multiple studies to examine IOPs. This is only truly possible by coupling the returned signal with bio-optical modeling to aid in resolution of optical properties (Churnside and Donaghay 2016; Churnside et al. 2014; Churnside and Marchbanks 2015). Unlike atmospheric lidar applications it is necessary to use some form of modelling to aid in retrievals due to the complexity of the returned signal.

A more complex approach comparing Monte-Carlo modeling and measured data is being deployed by multiple groups (Liu et al. 2019; Zhou et al. 2019; E. Zege et al. 2007). This approach may provide the best methodology for determining appropriate methods to tease out the impact of IOPs from the lidar signal. With the complexity of ocean waters, continued investigation coupling modeling with measured data provides the strongest methodology for the generation of lidar inversion techniques.

1.3 Lidar Basics and Components

A lidar system consists of a source laser, telescope and computer system. A basic bistatic lidar system can be seen in Figure 1.1. Following the system from source to receiver, short pulses of light are generated by the laser. Each packet of light is emitted from the laser, reformed through expansion, shape correction and filtering optics and then enters the medium. These light packets then scatter off particles and density discontinuities leading to some portion of this scattered light making it back to the telescope as a function of distance derived from time-of-flight. At the focal point of the telescope is a sensitive detector, in many cases, a photomultiplier tube (PMT) which is turned on and off in order to measure the returned light as a function of time (distance). The radiant energy is then amplified and measured by the PMT, which is subsequently measured as current, digitized and stored in the computer system. Depending on the application of the lidar the received light can be filtered to allow measurement of specific wavelengths and polarization states. The saved data is range gated using the distance, and width of the pulse, providing the intensity per unit distance. System geometry, wavelength and pulse width of the laser used are all dependent on the application.

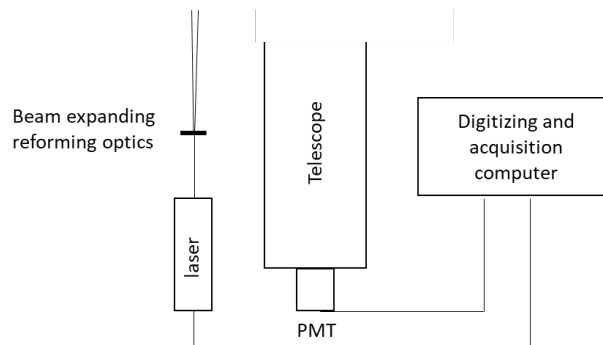


Figure 1.1: General schematic of lidar system.

1.3.1 PMT

Photomultiplier tubes amplify a small photon flux into a measurable signal. PMTs use a combination of the photoelectric and secondary emission effects of photons and electrons. The photoelectric effect was first discovered by Hertz (1887) and expanded upon by Albert Einstein in 1905 Einstein (1905). This is basically where the emission of electrons is stimulated by incident electromagnetic radiation. This effect is then coupled with the secondary emission effect, where electrons can cause the emission of additional electrons by hitting a charged electrode in a vacuum tube. This effect was first reported in 1899 by Paul Villard, but was matured as a concept for measurement by Joseph Slepian in 1919. Photons hitting the front of a PMT pass through an input glass window and excite electrons in a photocathode. This emits photoelectrons into a vacuum tube. Inside the vacuum tube are focusing electrodes and dynodes. The photoelectrons hit the initial dynode and then undergo repeated secondary emissions of electrons down a series of dynodes. This region of the PMT is aptly referred to as the Electron Multiplier. This region amplifies the signal generated by the original photon flux by a factor of 10^6 to 10^7 (Hamamatsu 2017). The signal is then measured at an exit anode.

1.3.2 Digitizers

Digitizers are similar in function to a digital storage oscilloscope. Digitizers take an analog signal from a measuring device and convert it to a digital signal. Digitizers can modulate their frequency for fast measurements. Oceanic lidars require fast digitizers (> 250 MHz) to allow for appropriate time resolution for profiling (Churnside 2001). AC coupling of digitizers can also be employed to aid in removing the effects of ambient light and other extraneous signals by filtering out non-zero mean steady state DC signals. The

digitizer also controls the dynamic range of a system. In lidar applications, large dynamic ranges are necessary to properly retrieve signals across the entirety of a profile. Two methods to improve signal dynamic range include splitting signals into high and low-gain channels and by using logarithmic amplifiers. By splitting a signal into high and low-gain channels it is possible to digitize the two channels separately and bin them together in processing. Dynamic-range compression uses a logarithmic amplifier to increase PMT gain, with time, to match signal decay or to use a feedback circuit to obtain a logarithmic response. These are all difficult due to the high frequencies required.

1.3.3 Lasers

In May 1960 Ted Maiman surrounded a cylindrical ruby rod with a strong xenon flash lamp used in photography. The flash lamp then pumped so much energy into the ruby rod that a population inversion occurred in the energy state of the electrons, meaning that there are more excited electrons than there are at ground state. As the excited population returns to ground state, photons are released. The photons emitted within the crystal induce other electrons to raise to higher energy states increasing the number of photons produced through a phenomenon called stimulated emission. The light generated is coherent, meaning that the peaks and troughs of the emitted light line up. The edges of the ruby crystal were made incredibly parallel with an error of less than 2 nm. Both ends of the crystal were mirrored. This means that all light that does not line up with the axis of the cylinder are emitted through the sides of the crystal and the light parallel to the axis is intensified and has a narrower spectral distribution. Standing waves form within the crystal in accordance with the rod length also help to produce a coherent single wavelength with high intensity. Finally, one end of the crystal can have a small hole or can be partially

silvered to allow light to be emitted. Thus this provided the three properties of laser light which are a coherent, collimated and monochromatic beam (Maiman 1960). Although there are many forms of lasers that exist today, they all follow this general concept in their function.

With the advent of improved technologies and techniques in chemistry and electro-optical systems, new specialized crystals, glasses, gasses, pumping sources and techniques like Q-switching and frequency doubling all allow for a wide range of power and wavelength characteristics in modern lasers in sizes not possible in the 1960s. One such crystal common in solid state lasers is Nd:YAG (neodymium-doped yttrium aluminum garnet; $\text{Nd:Y}_3\text{Al}_5\text{O}_{12}$). This crystal, when pumped with a flashtube or a laser diode commonly generates a beam at 1064 nm. Q-switching is where an optical switch is inserted into the laser cavity. This can be done both passively and actively. Passive Q-switching uses a saturable absorber where active Q-switching uses a modulator. At the point of maximum population inversion, the switch figuratively “opens” allowing the light wave to travel through into the cavity, depopulating the excited laser medium. This provides large output powers and also can help to reduce the pulse duration of a laser. Frequency doubling is a nonlinear process where two photons with the same frequency can interact with a material and are combined to produce a photon with twice the energy: effectively doubling the frequency and halving the wavelength.

DPSS (diode-pumped solid state) lasers are made by pumping a solid gain medium, like a Nd:YAG crystal, with a laser diode providing for high power lasers which can be configured in many different wavelengths in a small package. The wavelength of the pumping laser diode is tuned using temperature and is a compromise between absorption

of the crystal and the energy required for lasing. A single crystal can be stimulated by a grid of laser diodes by removing the dark areas between the diodes, creating a more complete lasing of the crystal leading to greater average power. DPSS lasers are very small but can provide a large amount of energy and come in many wavelength, power and pulse width specifications, making them a good candidate for compact oceanic lidar systems.

The most commonly used laser source in ocean lidar applications is a Q-switched frequency-doubled Nd:YAG laser producing a 532 nm beam with a pulse width of 1 to 10 ns. Due to the availability of small, efficient and rugged lasers at 532 nm this wavelength is commonly chosen (Churnside 2013). 532 nm also coincides with the region of highest light penetration in most ocean waters (Chen et al. 2019). This green region of the electromagnetic spectrum is a minimum for absorption when considering all of its components: water, particles and CDOM where scattering is spatially flat. Water absorption is much larger for red light than for blue light. Using three common wavelengths of solid state lasers, 473, 532 and 650 nm, $a_w(532)$ is about 4 times larger and $a_w(650)$ is roughly 9 times larger than 532. Although absorption from particles and CDOM both follow a general exponential decrease from blue to red, this coupled with the absorption of water creates a minimum in the green wavelengths.

1.3.4 The Single Scatter Lidar Equation

The single scatter lidar equation is comprised of four factors. 1 summarizes the performance of the lidar, 2 describes the geometry as a function of range, 3 describes the backscattering as it changes with distance and 4 deals with the transmission of the laser pulse as it propagates through the measurement medium. The first term (C) describes the measurement characteristics of the lidar system.

$$p(r) = C \frac{\beta_{\pi}(r)}{r^2} \exp \left[-2 \int_0^r K_{sys}(r') dr' \right] \quad (1-4)$$

C includes the initial laser power, the area of the receiving optics, the source divergence, the impulse response and the function which defines the overlap between receiver and source. The two optical parameters which describe the magnitude of the returns are the angular scattering coefficient at 180° ($\beta_{\pi}(r)$) and the Lidar attenuation ($K_{sys}(r)$). The single scatter lidar equation assumes that the photons measured by the lidar have only undergone one scattering event backwards towards the detector. The photon then undergoes both absorption and scattering along the path to and from the lidar. Multiple scattering is not considered in this form and is therefore a problem when making measurements in turbid waters. Multiple scattering decreases the slope of the lidar return ($K_{sys}(r)$) as $p(r)$ is larger at each distance. Techniques to incorporate multiple wavelengths (Gray et al. 2015) and multiple fields of view (Feygels et al. 2003), show promise in strengthening retrievals of IOPs by providing analytical solutions to the lidar equation by decreasing the number of unknowns.

Determination of attenuation from the lidar backscattered return is conducted using the slope method. This method looks at the derivative of the log transformed single scatter lidar equation after that signal has had the effects of the inverse square law accounted for in the signal as a function of distance. Nine assumptions which make the slope method viable are: (1) Incoherent scattering: wavelets have random relative phases in the backward direction; (2) Emission (fluorescence) or ambient light is much smaller than the backscattered laser light at the wavelength in question; (3) Only backscattered light is received; (4) There is an even light distribution over the effective area of the detector; (5)

No pulse stretching; (6) Complete overlap of source beam by receiving optics ($1/r^2$); (7) Constant phase function over small solid angles within the sample volume i.e. homogeneity within the laser path to and from the lidar; (8) Particles do not shadow one another, i.e. particles do not remove light from following particles. and (9) The light source is monochromatic (Evans 1984). With these assumptions, the lidar equation can be simplified and inverted as follows:

$$K_{sys} = -\frac{1}{2} \frac{d}{dr} \ln[p(r) * r^2] \quad (1-5)$$

To account for the two way travel of photons to and from the lidar the derivative is divided by two. Range correction accounts for the quadratic loss of light with distance by multiplying the signal at each distance by r^2 . The calculated K_{sys} will fall between k_d and c . Narrower fields of view and laser divergences lend themselves to better determination of c , while larger fields of view and laser divergences invert closer to the downwelling attenuation coefficient (Walker and McLean 1999). This is due to large fields of view collecting more light that has both been singly and multiply scattered, making the measurement defined more by the absorption than attenuation. Wide fields of view also broaden the response through a shift to shorter wavelengths (Walker and McLean 1999).

Attempts to isolate multiple scattering within the lidar equation have been undertaken using Monte-Carlo (Kattawar and Plass 1972; E. P. Zege, Katsev, and Prikhach 2007) and Small Angle Approximation (SAA) (Katsev et al. 1997). These methods mostly require *a priori* information like the single scattering albedo and/or volume scattering functions to achieve good performance. For autonomous or near real-time measuring systems the significant amount of power and computation required is not necessarily

available. It is for this reason that the inversion of the singly scattered lidar signal is being investigated.

1.4 Metron Backscatter Waveform Calculation

The EODES (Electro-Optical Detection Simulator) Monte-Carlo code developed by Metron is a multifunction modelling tool built to aid in designing and simulating underwater lidar signals. This computational model incorporates both system hardware and water optical properties. Within this code is a module designed to generate the backscattered returns from the water column. Using this code it is possible to examine the effects that different lidar configurations such as field of view, beam divergence, wavelength, and optical properties of the medium have on performance.

The inputs for Metron can be split into two categories: IOPs and lidar characteristics. For IOPs the model parameters are the attenuation, scattering, phase function and β_π . A schematic showing the geometry of the lidar system are found in Figure 1.2. The geometric characteristics of the lidar are the source receiver separation (SR), the source divergence (α_s), the transmissivity of the source lens (T_s), the collector area (A_c), the angle between the source and receiver primary axis (θ_c), the collector aperture half angle (α_c) and the transmissivity of the collector lens (T_c). A final input to account for the properties of the source beam are a scaled pulse which accounts for the pulse repetition rate, pulse width and average power

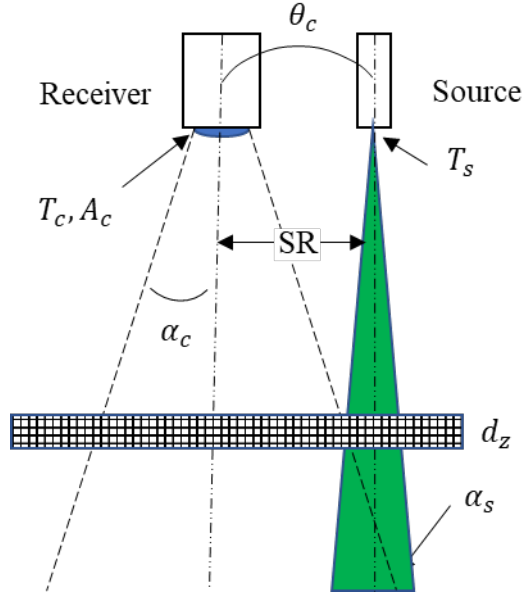


Figure 1.2: Schematic showing lidar geometric arrangement in Metron backscatter model.

The backscatter module calculates the time-dependent returns due to scattering as a function of distance in the object plane (Giddings and Shirron 2009). The model generates a pulse of laser light which is a narrow beam, and a narrow field of view pointed in θ_c . As a plane-stratified problem the position of the laser in space is uncoupled from a single layer, as would be the case with an imaging application, and instead into a time-dependent power term and spatio-angular function. The optical paths are limited to small-angle forward scattering and a single large-angle scattering event backwards (De Wolf 1971). The medium is discretized into slabs of finite thickness (dz), matching the beam characteristics, perpendicular to the direction of the beam. Each return is handled similarly to a hard return from a plane by convolving the systems spatial impulse response with the reflectivity of the slab. The spatial response is determined via the small-angle scattering approximation and the radiative transfer equation to provide the returned pulse energy at each distance.

The geometry of the system has the largest impact on the ability of the lidar to isolate different IOPs. The backscatter module is utilized to model time-dependent

backscattering returns for given IOPs and geometry of a lidar system. This will allow extensive testing of different lidar geometries, aiding in the design of appropriate of both lidars and inversion techniques for determination of optical properties. This can also provide a foreword solution in the form of look up tables (LUT) for fast processing in the field.

1.5 Lidar Backscatter Waveform Interpretation

Lidar backscatter waveforms show the distribution of returned power as a function of distance from the sensor. For bistatic lidar systems the area closest to the lidar is dominated by multiple scattering as the source and receiver have not overlapped. Meaning that any light received by the sensor has undergone multiple interactions to scatter backwards towards the receiver field of view. Once the receiver field of view encompasses the laser pulses it causes a peak in the energy returned, this region is called the common volume. The magnitude of backscattered light then decreases as a function of the inverse square law coupled with the optical properties of the medium. To remove the effects of the inverse square law range correction is applied. In its simplest form range correction is the multiplication of the returned power at each distance by the distance squared. The slope of the common volume is K_{sys} . Understanding the interplay between the energy received in both regions can aid in initial determination of the attenuation close to the sensor face (Strait et al. 2018). This is a potential method for removing uncertainty in parameterization when solving the lidar equation.

For a constant particle population across the lidar sample volume, the returned power as a function of distance should be linear after the common volume in log space (Figure 1.3i), i.e. K_{sys} is constant over the measurement range. The linear decrease in the

power with distance is simple to determine in this case using derivatives. Boundaries on the first and second derivative can help isolate the most linear region of the scan.

With the particle population consistent if a waveform changes slope over its measurement volume (Figure 1.3ii), an incomplete understanding of the electro-optical response of the lidar must be assumed. In this case determining appropriate regions over which to measure the slope becomes more difficult. Methods to determine linear regions then require a mix of geometric positions and intensities be incorporated into the discrimination of linearity in order to isolate the best candidate for slope measurement. Furthermore, the truncated measurement region may also be affected by the same electro-optical errors to a greater extent than is apparent. Especially with measured data, digitization noise can also impart large first and second derivatives, obfuscating regions of interest and complicating their determination. The cause of malformations due to lidar characterization must be quantified and corrected in order to obtain accurate slopes.

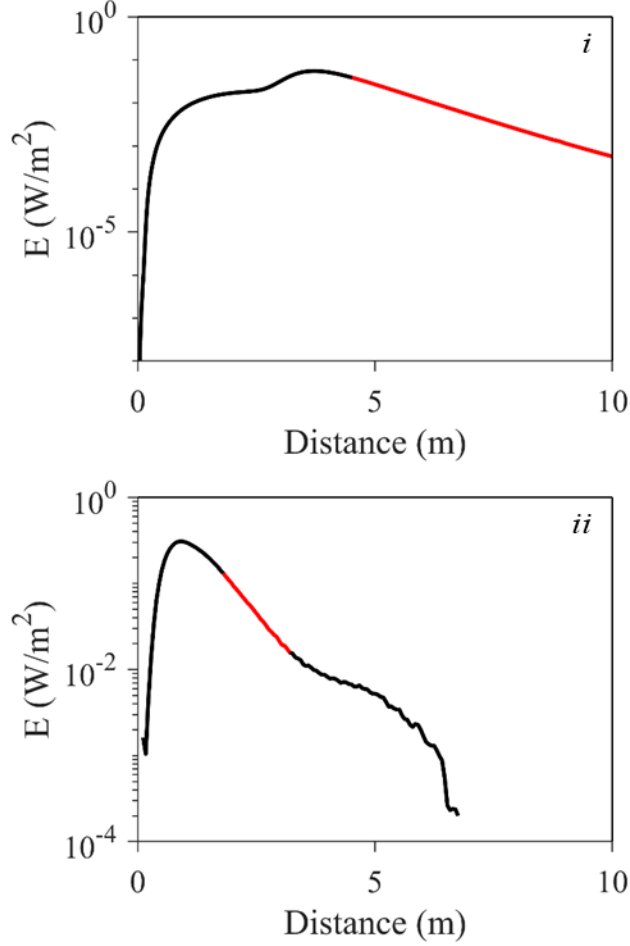


Figure 1.3: Example of a good waveform (i) and example of a malformed waveform (ii). Black lines are the waveform while the red lines are the linear regions over which the slope is calculated.

Gordon (1982) used Monte-Carlo modelling of airborne lidar waveforms with multiple scattering to examine the effect of geometry on inversion for attenuation. The lidar source characteristics were modelled after the NASA AOL lidar. The single scatter albedo was used to manipulate the magnitude of the IOPs through 4 steps ($\omega_0 = \frac{b}{c}$; 0.3 to 0.9 by 0.2). The single scatter albedo also defined the relationship between the two unknowns in the single scatter lidar equation β_π and c . The relationship found for calculating K_{sys} is as follows:

$$K_{sys} = k_d + (c - k_d)\exp(-0.85 * cD) \quad (1-6)$$

Where the diffuse attenuation coefficient was calculated from absorption and backscattering, and (D) is the spot size at the air-sea interface and is a function of the height of the lidar. Gordon compared the attenuation and the spot size of the field of view at the surface of the ocean to ratios of $\frac{K_{sys}}{c}$ (reproduced from Gordon (1982); Figure 1.4). This coupled the geometry of the lidar system to the capabilities of the lidar to invert for c . It was found that the spot size had a large impact on the retrieval of the system. The asymptotic region in the approximation are due to the shift from a single to multiple scattering regime.

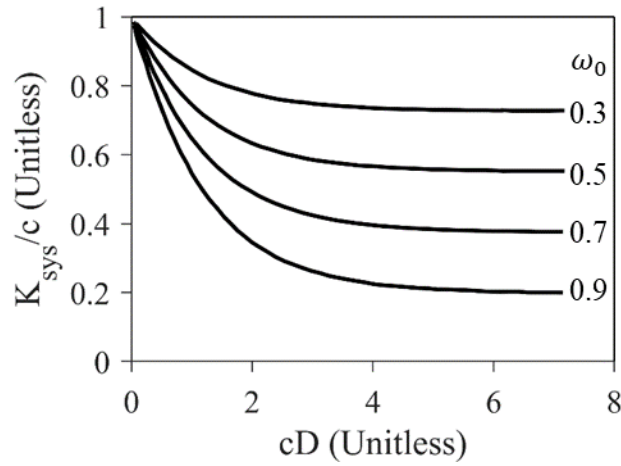


Figure 1.4: Gordon approximation from Monte-Carlo simulations of lidar attenuation coefficients normalized by the attenuation. Single scatter albedo showing for each calculation reported from Gordon (1982).

2 Forward Modeling for Investigation into Inversion Approaches

2.1 Introduction

The single scatter lidar equation has two unknowns $\beta_{\pi}(r)$ and $K_{sys}(r)$. Attempting to invert a lidar waveform for either of these parameters requires *a priori* knowledge or assumptions about the nature of the other. It is for this reason that any inversion regime will require some coupling between independent measurements or modeling and the lidar signal to be effective.

Building lidar systems with sufficient flexibility to change geometries in the field is a complicated and expensive endeavor, especially within relatively compact profiling lidar packages. Proper characterization of such a system also becomes quite complicated and leads to errors in inversion. Modeling provides a space through which many independent lidar systems can be tested under various IOPs in order to comprehensively investigate inversion techniques. Monte-Carlo modeling has the advantage of including multiple scattering, providing for more robust inversion.

A synthetic dataset was created in order to test lidar inversion across a wide range of IOPs, which represent the majority of ocean waters. Ultimately there were 1500 IOP conditions. Four lidar fields of view were then tested using the synthetic dataset. With this a relationship between lidar geometry and an inversion formulation could be explored. The model also provides an idealized lidar system with infinite bandwidth and a perfectly

efficient detector. This removes the ambiguity imparted by the characteristics of lidar hardware.

2.2 Methods and Materials

2.2.1 *Synthetic Dataset Creation*

Figure 2.1 shows a schematic view of the optical inputs for the EODES backscattering module. In order to generate a realistic set of optical inputs a synthetic dataset must be created which can account for the range of IOP situations that can be seen in the ocean.

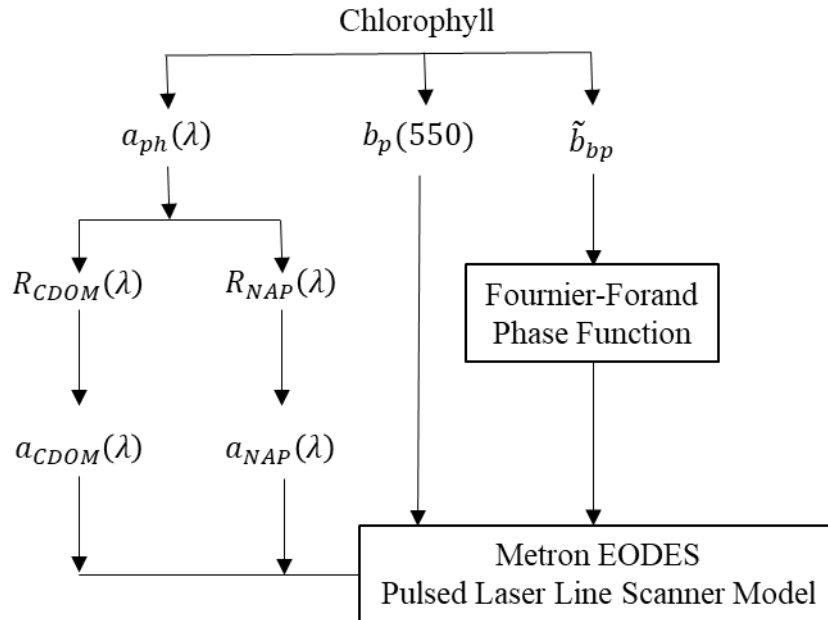


Figure 2.1: Schematic view of Metron backscattering module inputs.

In order to cover most natural waters 20 chlorophyll concentrations between 0.01 and 30 $\mu g L^{-1}$ were generated. A logarithmic distribution of concentrations was selected to both reduce the total number of cases being examined, as well as more appropriately weigh the number of cases to lower concentrations which are more prevalent in nature.

Calculation of IOPs from chlorophyll follows the Case 1 assumption: that optical properties of the ocean covary with respect to chlorophyll concentration (Morel 1988).

2.2.1.1 Phytoplankton Absorption

A method for calculating phytoplankton absorption spectra using chlorophyll normalized pico and micro plankton spectra was presented in two papers (Á. M. Ciotti, Lewis, and Cullen 2002; A. M. Ciotti and Bricaud 2006):

$$a_{ph}(\lambda) = [Chl] * ([S_f * \bar{a}_{<pico>}(\lambda)] + [(1 - S_f) * \bar{a}_{<micro>}(\lambda)]) \quad (2-1)$$

Here, basis values (S) are constrained between 0 and 1 and specify the relative contributions of picoplankton and microplankton to absorption. Generation of spectra is possible using information from Ciotti (Á. M. Ciotti, Lewis, and Cullen 2002), where normalized micro and picoplankton spectra were determined for every 2 nm from 400-640 nm. Three basis values are used to best cover the range of picoplankton and microplankton found in natural waters $S_f = [0.25 \ 0.5 \ 0.75]$.

Phytoplankton absorption was calculated for the two laser wavelengths 473 and 532.

2.2.1.2 Non-Algal Absorption

To determine the non-algal portion of absorption, Lee (IOCCG 2006) randomly picks ratios of $R_{NAP} = \frac{a_{NAP}(440)}{a_{ph}(440)}$ between 0.006 and 1.7 to determine the NAP absorption from the chlorophyll derived a_{ph} at 440nm. Rather than selecting ratios, five values were randomly selected $R_{NAP} = [0.05, 0.1, 0.5, 1, 2]$. To determine a_{NAP} at each of the two laser wavelengths, a fixed slope (S_{NAP}) of 0.011 based off of Roesler and Perry (1995) and is used in equation 10:

$$a_{NAP}(\lambda) = a_{NAP}(440) * R_{NAP} * \exp^{-S_{NAP}(\lambda-440)} \quad (2-2)$$

2.2.1.3 CDOM Absorption

CDOM absorption was calculated similarly to NAP using:

$$a_{CDOM}(\lambda) = a_{ph}(440) * R_{CDOM} * \exp^{-S_g(\lambda-440)} \quad (2-3)$$

The ratio $R_{CDOM} = \frac{a_g(440)}{a_{ph}(440)}$ is varied by Lee within the range 0.11 and 5.5. As with

NAP five ratio values were considered for CDOM: $R_{CDOM} = [0.1, 0.3, 0.5, 1, 2]$. The slope (S_g) was fixed at 0.014, appropriate for the 473 – 532 nm range.

2.2.1.4 Particulate scattering coefficient

Total scattering is required as an input to determine the phase function and the downwelling extinction coefficient for oceanic waters. The particulate fraction of scattering is calculated at 550 nm with (Loisel and Morel 1998):

$$b_p(550) = 0.416[Chl]^{0.766} \quad (2-4)$$

b_p can be propagated spectrally using the relationship developed by Morel (Morel 2009):

$$b_p([Chl], \lambda) = \left(\frac{\lambda}{550} \right)^{v([Chl])} b_p(550)([Chl]) \quad (2-5)$$

The exponent v is related to the size distribution function and was found to be between -0.3 and -1.7. Larger particle assemblages will be closer to -0.3 while smaller particle populations will be closer to -1.7. A varying exponent was proposed by Morel, Antoine, and Gentili (2002) and is dependent on chlorophyll in this way:

$$\begin{aligned} v([Chl]) &= \left(\frac{1}{2} \right) (\log_{10}[Chl] - 0.3) \\ &\text{when } 0.02 < [Chl] < 2 \text{ mg m}^{-3} \\ v &= 0 \text{ when } [Chl] > 2 \text{ mg m}^{-3} \end{aligned} \quad (2-6)$$

To obtain b_t , b_w was calculated with a salinity of zero and a temperature of 25°C using Zhang, Hu, and He (2009).

The particulate backscattering ratio (\tilde{b}_{bp}) was related to chlorophyll by Twardowski (2001).

$$\tilde{b}_{bp} = \frac{b_{bp}}{b_p} = 0.0096[Chl]^{-0.253} \quad (2-7)$$

This relationship covered a range of chlorophylls from 0.1 to 10 $mg\ m^{-3}$. The correlation coefficient for this was 0.52. Other models were also tested and were not as predictive of \tilde{b}_{bp} . At low \tilde{b}_{bp} (low refractive index (\bar{n}_p), high chlorophyll) algal particles dominate the scattering properties and the relationship is stronger. However, in Case II waters this tends not to be the case due to terrigenous (inorganic particulate) influence over the particle population.

Fournier and Forand (1994) calculated phase function from \tilde{b}_{bp} . This is calculable using the method of Mobley et al. (2002). By using the Fournier-Forand method, the phase functions are coupled directly to chlorophyll-*a* and are closer to natural particle scattering that would be encountered in the environment. In all cases, the phase function of water was also included in the total phase function according and is calculated as a function of temperature (25°C) and wavelength (Zhang, Hu, and He 2009).

2.2.2 Geometric Model Inputs

With IOP inputs being produced by the synthetic dataset, geometric inputs were chosen to closely match the existing lidar at HBOI. Source receiver separation was 0.0606 m, the angle between the source and receiver optics was 0°. The source and receiver divergence and field of view respectively can be found in table 2.1. Nine fields of view

were ultimately tested, however only four were targeted for the final analysis due to their spread across the believable range of field of views. The area of the receiver was 2 cm² and the laser wavelength was 532. The transmissivity for both the source and receiver windows are assumed to be 100%. Geometry components for the source side of the system were kept consistent while the four fields of view were tested for each of the 1500 IOPs. Each Monte Carlo run used 2E⁶ photons.

Table 2.1: Geometry for Metron Model Runs in Half Angle.

α_s (rad)	α_c (rad)
0.002	0.0045
0.002	0.0085
0.002	0.0435
0.002	0.0875

2.2.3 Slope Calculation

Waveforms were range corrected and the natural logarithm applied in accordance with equation 2. Waveform slopes were calculated by detecting linear regions of the waveforms using the first and second derivative. The geometric common volume is used as a discriminator between the beginnings of the measurable region. Since these waveforms are idealized calculating slopes was relatively simple.

2.2.4 Inversion Using Modified Gordon Methodology

The K_{sys} was compared with attenuation in accordance with the Gordon (1982) analysis. Like in the analysis by Gordon, the relationship of $\frac{K_{sys}}{c}$ was used, however since there is no spot size at the air sea interface as there was in his work, the R term was set to 1 for all scans. This relationship was then fit using multiple regression analysis to find the most appropriate fit given the *a priori* information at hand. Results that had ratio values

above one were removed to aid in the fitting process. While Gordon does show that there are some conditions where this was true in his model, this should be impossible as it infers that the slope of the lidar return is not affected by attenuation.

Data was binned by the albedo following the approach of Gordon (1982). Ten fitting formulas were attempted both with and without *a priori* IOPs being used. The function which had the greatest accuracy while fitting was:

$$\frac{K_{sys}}{c} = \frac{A}{c} + (B\omega)\exp(-Gc) \quad (2-8)$$

where A, B, and G were the fitting components. G is considered the geometry component of the function. This fit then allows for extrapolation of lidar measurements to include multiple receiver field of views. With an appropriate fitting regime was established for the $\frac{K_{sys}}{c}$ vs c relationship, a geometry function was then determined between FOV and G .

2.3 Results

The Metron Backscattering Model, properly calibrated, can provide a vehicle for generation of waveforms for realistic optical properties. The Metron model has a varied list of inputs which include the geometry of the lidar and the optical characteristics of the medium. By generating a large range of optical characteristics it was then possible to model the influence that geometry had on the returned waveforms.

The chlorophyll concentration ranged from 0.01 to 30 μgL^{-1} . Each chlorophyll concentration in the synthetic dataset produced 75 iterations. With this a total of 1500 unique IOP situations could be used in each of the model runs. The distribution also covered most of the observable range of IOP values. For 532nm absorption values ranged

from 0.0442-2.5824 and attenuation values ranged from 0.0602-8.2135. The distribution of single scattering albedos is shifted to higher values using this methodology with the majority between 0.75 and 0.95 (58%).

Twenty unique phase functions were determined from the backscattering ratio which in turn is directly calculable from chlorophyll. Figure 2.2 shows the distribution of Fournier-Forand phase functions with water included. Two phase functions were used during validation of this model: McClean-Freeman and one based on the scattering properties of Maalox[®] (Dalglish et al. 2008). To reduce errors in this modeling approach, the Fournier-Forand phase function was used to better represent conditions found in nature. Most of the input phase functions used previously also have not included water. Water was added to all phase functions used in this experiment.

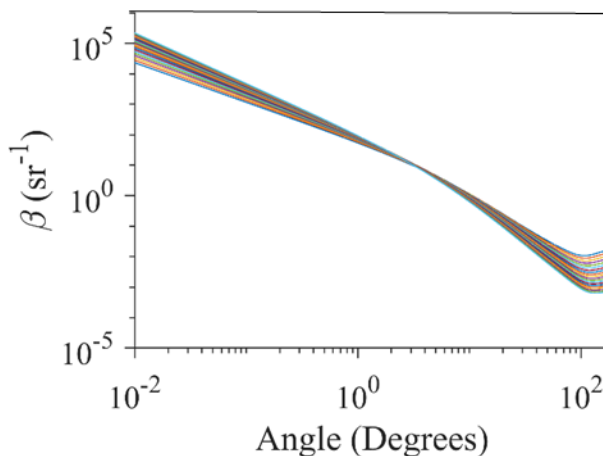


Figure 2.2: Fournier-Forand calculated phase functions derived from the backscattering ratio.

Changes in the IOPs and the field of view both have large impacts on the backscattered return to a lidar. Figure 2.3i shows examples of the changes in backscattering with respect to the attenuation and fields of view. The impact of IOPs on the backscattering return affects both the magnitude and the distribution of the returned light. It is noticeable

that as c increases the common volume peak shifts closer to the lidar. This is due to an increase in multiple scattering leading to a shortening of the distance to apparent overlap between the laser and telescope geometries. For very high b environments this can be almost instantaneous, which has implications for how well the single scattering lidar formula, and therefore the slope method, can be applied. This was not examined explicitly in this study, although it did lead to the removal of some slopes due to erroneously large values.

It is noticeable that in Figure 2.3ii that both the magnitude and noisiness of the returned signal is indicative of the light gathering capabilities of the lidar. Early into the investigation it was determined that 2 million photon bundles was an optimal choice to balance the time for each run and the noise level of waveforms. Increased errors in the smaller fields of view are most likely due to the probabilistic nature of Monte Carlo methodology. This has an impact as to whether or not the lidar can measure c or resolves closer to k_d , as the field of view becomes large more multiply scattered light is collected. The fields of views used here were constrained to small enough fields of view to allow for calculation of c rather than k_d .

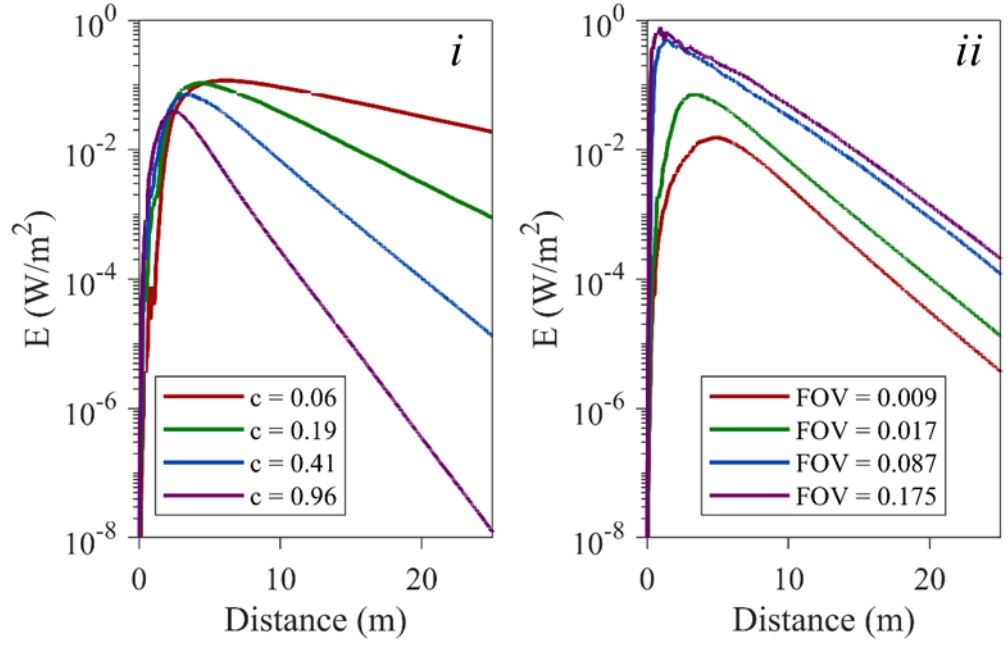


Figure 2.3: (i) Example waveforms with changing c for FOV 0.0175 rad, (ii) example waveforms with changing FOV at $c = 0.408 \text{ m}^{-1}$.

Slopes were calculated using the logic outlined in the methods. Because the receiver characteristics are idealized within the model, the calculation of the slope follows a simpler logic than with measured data. The high value of attenuation for some of the scans does bring into question the efficacy of using the slope method with more turbid waters. This did not have a detectable impact on the results.

A recreation of the Gordon plot is shown in Figure 2.4. The fundamental difference between this plot and the original relationship presented by Gordon (1982) is the setting of R , or the spot size on the water surface. Since the modelled system is a profiling lidar and does not interact with the air-sea interface R was set to 1. This was done to allow for comparison while acknowledging that this lidar system does not have an above-water component. This produces a similar relationship showing that the ability to calculate c diminishes asymptotically with increasing attenuation. As discussed in the original study,

this is likely due to the increase in multiple scattering and therefore, the shallowing of the lidar backscatter return with respect to c . The black lines are labelled with their respective chlorophyll concentrations while the individual curves made are based on the albedo binned at 0.2 increments. These curves were then fit using equation 9 along albedo curves and for each field of view separately.

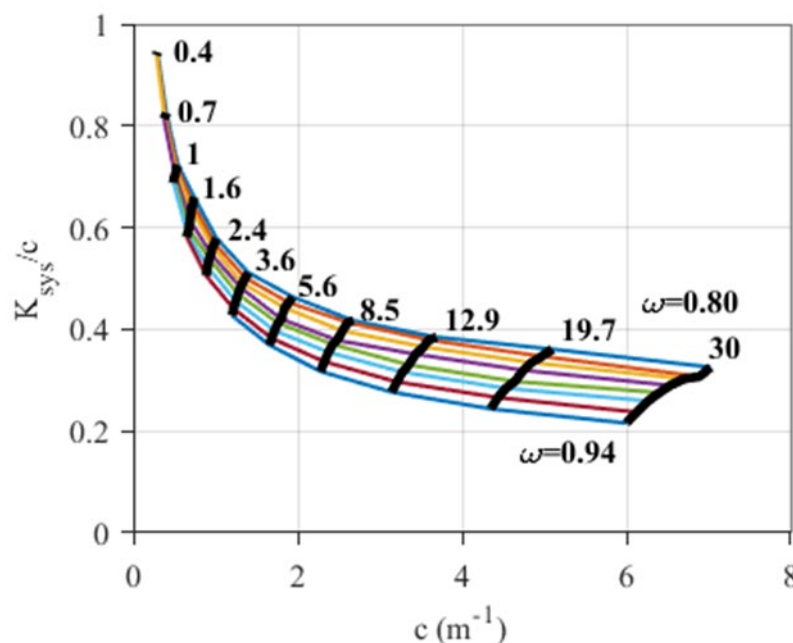


Figure 2.4: Example plot between c and $\frac{K_{sys}}{c}$ for all $[Chl]$ (black vertical lines) and for single scattering albedo (ω) binned by 0.0175 increments from 0.94 to 0.8.

The original fitting formula derived by Gordon involves k_d in its calculation. This was removed to limit the amount parameterization to only IOP values and constants. Figure 2.5 shows the results from fitting Equation 2.8 for each of the fields of view. A in the equation helps to define the asymptotic nature of the $\frac{K_{sys}}{c}$ relationship. It has a relatively constant value across different fields of view and albedos. The B parameter accounts for shifts in magnitude due to the single scatter albedo (Figure 2.5ii). Holding either A or B

constant in the fitting regime led to poor fitting results. Figure 2.5iv shows the mean root mean square error of all albedos for each field of view.

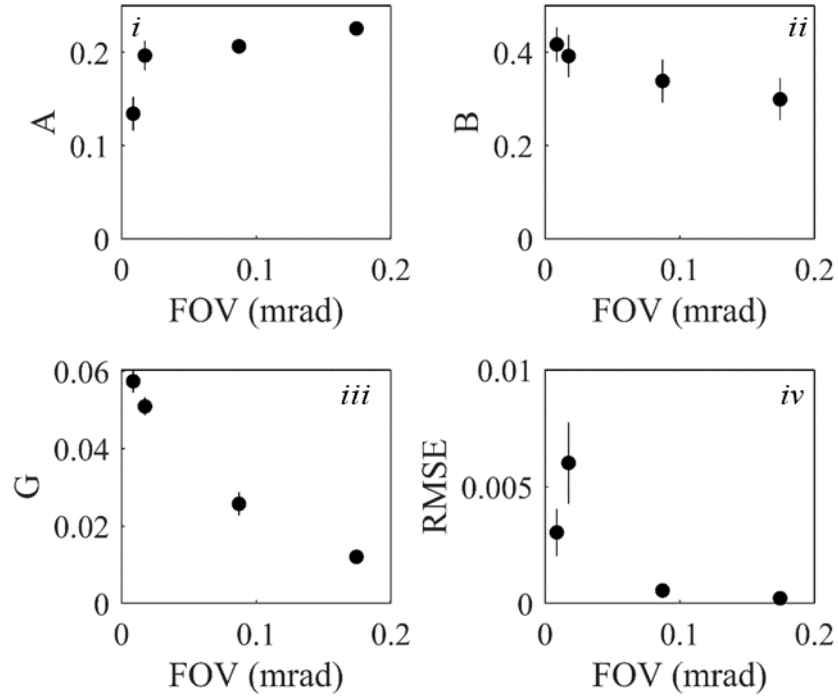


Figure 2.5: Fit coefficients for all albedos and fields of view. i, ii and iii show fitted coefficients for the three degrees of freedom in the equation. iv shows the goodness of fit through the root mean square error.

The relationship between field of view and G is shown in Figure 2.6. This dataset needs to be expanded to strengthen this relationship. The four fields of view were selected to cover the usable range of profiling lidar systems. An exponential decay curve was fit to calculate G from field of view $G = 0.061e^{-9.74*FOV}$.

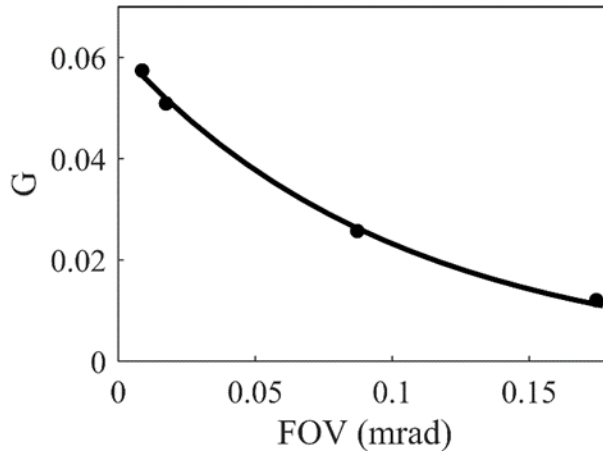


Figure 2.6: Fit between field of view and geometry component of equation.

2.4 Conclusion

With the geometry coefficient defined as a function of FOV, it is possible to generate waveforms for a series of lidar geometries. With this information, investigation into appropriate inversion algorithms can proceed. Development of look up tables to allow for real-time lidar inversion is also possible.

The Metron backscatter model provided a test bed for lidar waveform generation utilizing 4 fields of view and a synthetic dataset. The Gordon inversion technique was tested with the geometry of a profiling lidar showing promise. The inversion required only c and ω_0 as *a priori* input. With an understanding of ω_0 it is possible to determine attenuation to roughly 3 m^{-1} before the inversion becomes asymptotic. Full parameterization of A and B is still required. While A remained relatively constant B had large standard deviations. Holding of A and B constant across fields of view did not closer fits. An expansion on the number of single scattering albedos may show a failure in this inversion as absorption increases. Too few albedos below 0.75 were present in the dataset

to make a determination on this point. Further fields of view and model validation with a known system would aid in supporting this method.

3 Characterization of Lidar Systems

3.1 Introduction

Inversion of lidar backscattered signal requires strong characterization of the lidar. Without an adequate understanding of the power, geometry and receiver characteristics of lidar systems, $p(r)$ will not be coupled to just IOPs but also the measurement characteristics of the lidar system, making inversion impossible. To account for this rigorous characterization of the C term in the single scatter lidar equation is required:

$$C = P_0 \frac{c\tau}{2} A\eta \frac{O(r)}{r^2} \quad (3-1)$$

Here P_0 is the initial laser power, c is the speed of light in water, τ is the laser pulse width, A is the area of the receiving optics and η is the overall system efficiency. The system efficiency describes the efficiency of all of the elements of the source and receiver optics as well as the efficiency of the detector. The overlap function (O) takes into account the receiver field of view, laser beam diameter, shape, divergence and the positions and angles of the source and receiver optics with respect to one another. It defines the overall proportion of the light scattered into the solid angle of the receiver at each distance. At the face of the lidar $O = 0$ and goes to a maximum of $O = 1$ once the laser and receiver optics lie at unity.

Without a precise characterization of the C term in the lidar equation, changes in signal due to IOPs may not be discernable within the backscatter waveforms.

Malformations in the waveform signal can be due to many issues stemming from a poor understanding of how the lidar will react to a signal.

3.2 Methods and Materials

3.2.1 *HBOI lidars*

Two identical lidar systems were developed under NOAA-OAR funding and underwent testing at Florida Atlantic University Harbor Branch Oceanographic Institute, called SN1 and SN2. SN1 was built to be integrated into the NOAA PMEL Oculus Coastal Glider while SN2 was to be integrated into systems at Harbor Branch. Both units weigh approximately 37 pounds in air and have small power draw (~45 Watts). They are eye safe systems which include both blue and green Bright Solutions DPSS passively Q-Switched pulsed laser sources (473 and 532nm respectively). These have pulse energies of $16 \mu J$ and $20.1 \mu J$ and pulse durations of 1.2 ns and 1.26 ns for blue and green respectively. The repetition rate for each laser is 100 Hz. Both systems are bistatic lidars with a small separation between the receivers and source of 6.06 cm. They each have two receivers, both with the same acceptance angle and distance from the source, but at different orientations with respect to the source. One is considered on axis and measures down the same axis as the exit beam ($\theta_c = 0^\circ$). The second channel (off axis, $\theta_c = 10^\circ$) provides a view of the multiple scattered signal before the common volume (Vuorenkoski et al. 2015). These systems have a vertical resolution of 5.625 cm. Each measurement is the average of at least 100 seconds of collection giving ten thousand scans per measurement.

Figure 3.1 shows the 3D model of the lidar highlighting multiple key systems in the source and receiver optics with the digitizer. The source plate holds the electronics and laser components, where the telescope assemblies are affixed to the outer chassis.

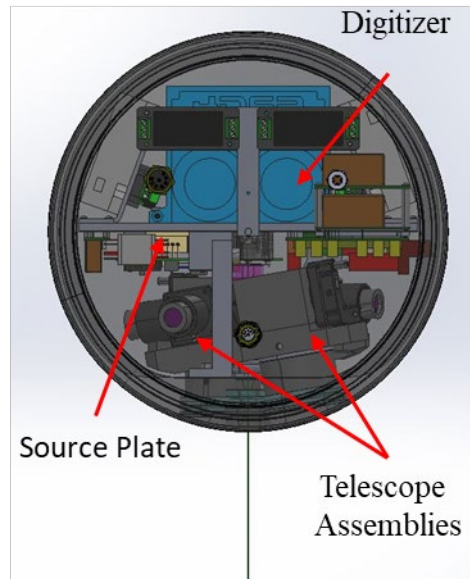


Figure 3.1: Side view of lidar system. Both SN1 and SN2 are identical, save for aperture and laser settings.

Figure 3.2 shows the laser stage with only the lasers and combining optics. The lasers emit perpendicular to one another, within the combining optics compact lenses are used to correct any asymmetries or aberrations in the beam shape. These lenses also help are used to expand the beams to the desired divergence. The two lasers are then combined and exit together through a mirror perpendicular to the source plate.

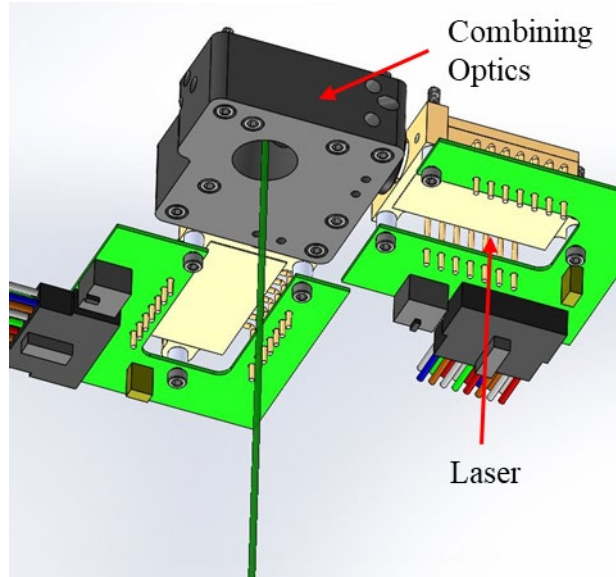


Figure 3.2: Source components showing both laser and beam combining optics.

To ensure that the digitizer couples the PMT signal appropriately with laser pulses, a trigger is used to initiate measurement of the exiting beams. The two lasers pulse sequentially reducing interference between the two. Figure 3.3 shows the trigger tube (purple) sitting between combining optics and the exit window. A small lens was installed in the tube which reflects less than 1% of the laser light towards a sensitive photodiode. This measures the timing as the beams exit the unit and triggers the digitizer to start recording data from the PMTs on the telescope assemblies.

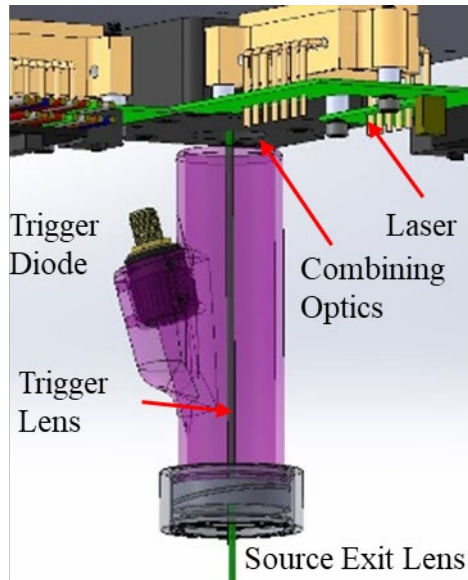


Figure 3.3: Trigger optics for both lidar systems.

Figure 3.4 shows the telescope assemblies. Each telescope has split PMT assemblies which incorporate a dichroic mirror to split the incoming signal into its two wavelength components. The reflected light then travels through a final bandpass filter before the PMT to reject ambient light.

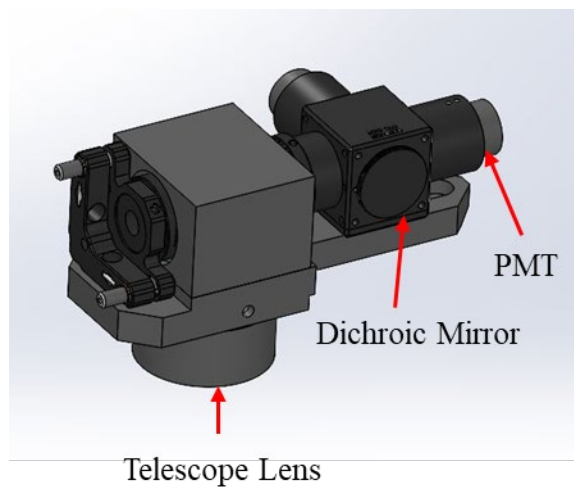


Figure 3.4: Lidar telescope assemblies.

Due to the production and breakdown of SN1, not all of the methods used to characterize SN2 were also used on SN1. Furthermore, initial indications from modelling

showed poorer results with SN2 than SN1, and therefore further characterization was necessary with SN2.

3.2.2 SN1 Field of View Characterization: a Baseline for Both Systems

SN1 was developed and characterized at the component level before the parts were integrated. The field of view of the telescope PMT assemblies was measured at multiple apertures using a phosphor lamp and rotating the assemblies using a Zaber stage. The lamp was moved perpendicular to the axis of the telescope with aperture settings of 2, 3, 5 and 10 mm apertures for both the blue and green PMTs.

3.2.3 Underwater Beam Divergence Measurement

Underwater measurements of beam divergence were conducted in the test tank range at HBOI. A mobile gantry was moved between three positions to allow the beam divergence to be measured at multiple places. The gantry is fitted with an encoder in order to precisely track its position. Images were taken using a Canon 5D Mark IV at each of the three locations. Multiple images were taken with multiple shutter speeds maintaining consistent apertures and ISO sensitivities. The aperture was selected to be small enough to provide decent depth of field in all of the images. By examining each of the images and producing an intensity profile it should be possible to measure the beam divergence.

Images were processed in Matlab. A reference image was taken with a dive light at each position. This was used to generate a checkerboard mask to isolate intensity changes caused by lighter regions of the target. This checkerboard mask also provides the size of each pixel for conversion to centimeters. A threshold was used to remove borders of the image and allow for profile generation. The point of maximum intensity was then selected

in order to extract a vertical and horizontal intensity profile. This profile was then fit with a Gaussian curve. Two points would then be used to calculate divergence following:

$$\theta = 2 \arctan\left(\frac{D_f - D_i}{2L}\right), \quad (3-2)$$

where L is the distance between the two points measured and D_f and D_i are the furthest and closest points to the lidar, respectively.

3.2.4 Above Water Laser Divergence Measurement

The laser divergence was measured using two techniques: a test bench with a graded reflector and a Gentec Beamage 3.0 beam profiling camera. The Beamage camera has a resolution capable of measuring beams down to $55 \mu m$ on a 2048×1088 pixel² CMOS sensor. The optical rail was set up in front of the lidar with the graded reflector or the profiling camera on a movable stage, as shown in Figure 3.5. Five positions were then selected from 5 mm to 1300 mm from the exit window to measure the divergence and search for a beam waist; two points were used for measurement of the divergence using Equation 3.2.

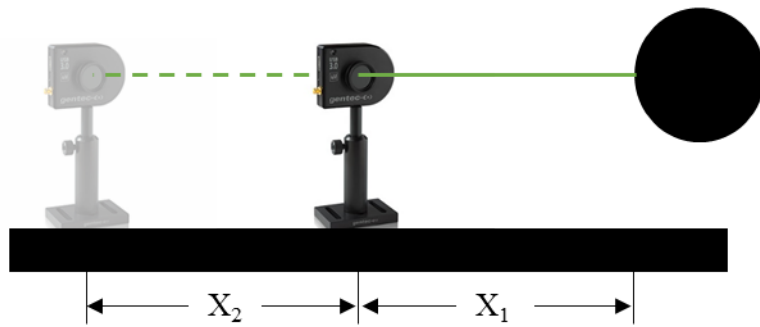


Figure 3.5: Setup for measuring beam divergence using Beamage 3.0 camera. X_1 and X_2 are the positions from the lidar which were measured.

3.2.5 SN2 Above Water Field of View Measurement

Due to the complexity of aiming the source laser, an external laser had to be used to measure the field of view. The external laser was aimed using two mirrors manually. Due to the external laser not being coupled with the digitizer, background DC current measurements were taken at discrete points on the reflector. Figure 3.6 shows the experimental setup:

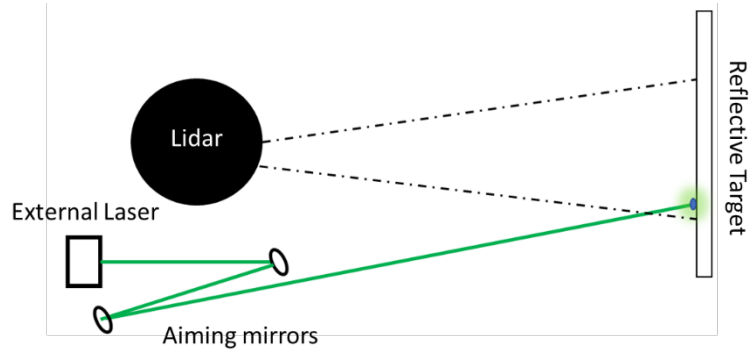


Figure 3.6: 3D in air field of View Setup.

The target was placed at 172.5 and 245.8 cm from the lidar output window. A background (dark) measurement was made for each point on the target by blocking the laser and all measurements were made in triplicate. This was done to account for any ambient light. The resulting intensity grid was then fit with a 2D Gaussian. This Gaussian was then used to determine the diameter of the beam at the full width half maximum. This was then propagated to distance 0 (exit window). From there, the field of view needed to have the difference in index of refraction applied using the vector form of Snells Law:

$$S_2 = \frac{n_a}{n_w} [\hat{N} \times (-\hat{N} \times \hat{S}_1)] - \hat{N} \sqrt{1 - \left(\frac{n_a}{n_w}\right)^2 (\hat{N} \times \hat{S}_1)(\hat{N} \times \hat{S}_1)}. \quad (3-3)$$

Here n_a and n_w are the indices of refraction for air and water respectively. \hat{N} is normal vector to the surface, S_1 and S_2 are the incident vector rays onto the refraction boundary.

3.2.6 SN2 PMT Linearity

To determine the linearity of the PMTs over the measurement range, a hard 25% spectralon target and 1.6 ND filter were used. The lidar was mounted out of the water and the intensity off of the target was measured for multiple PMT voltages (325-550 V). The use of ND filters helped provide the dynamic range required to measure across a wide range of PMT voltages.

3.3 Results

3.3.1 SN1 Field of View Characterization

Initial measurements of the lidar telescope and PMT system was measured using a phosphor lamp at multiple angles. Figure 3.7 shows the results from the field of view measurement. The larger the aperture the larger the field of view making the blue, orange, yellow and purple lines represent an aperture of 10, 5, 3 and 2mm respectively.

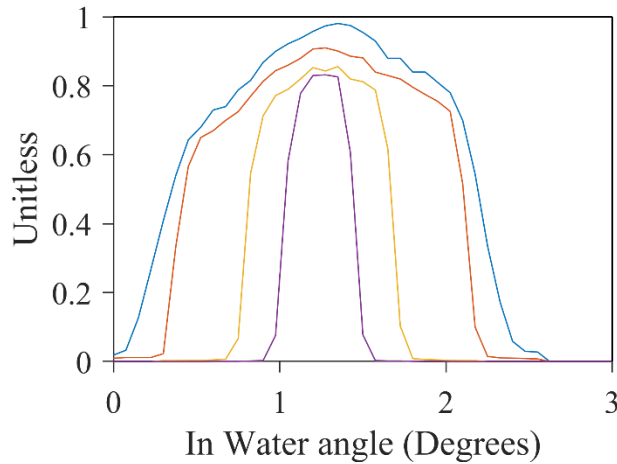


Figure 3.7: Field of views for aperture values 10mm (blue), 5mm (Orange), 3mm (yellow) and 2mm (purple).

SN1 had an aperture of 6mm leading to it having a field of view of 0.5 degrees half angle. SN2 started with a 10mm aperture giving it a perceived aperture of 1 degrees half

angle. Due to results from preliminary tests and model results it was decided that the field of view for SN2 required further verification.

3.3.2 Underwater Beam Divergence Characterization

Figure 3.8 shows an example image taken from the Canon 5D Mk IV of the green laser of SN1. As seen in the image the dynamic range of the camera made it difficult to fully image the beam without either removing the edges of the beam or oversaturating the image at the center of the beam. This led to large shifts in the size of the beam for changes in the settings for each picture. This also added to uncertainty in the fit of a Gaussian distribution to the reflected intensities. For SN2 this method was all but impossible as the size of the beam mixed with the dynamic range left an insufficient number of points to calculate a Gaussian shape.

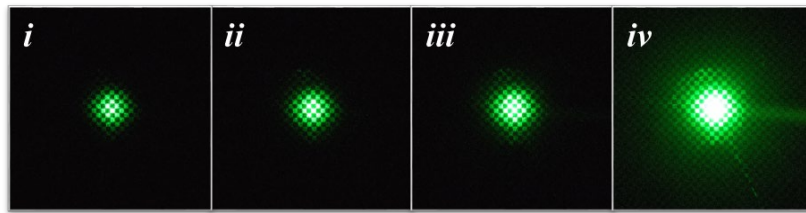


Figure 3.8: Difference in apparent divergence given changes in shutter speed. The f stop was set to $1/16$, the ISO was set to 10000 and the focal length was 40mm. The shutter speed was $1/8$, $1/4$, $1/2$ and 4 seconds for i, ii, iii and iv respectively.

Figure 3.9 shows a typical unmasked image. The checkerboard masking helps to zero out the black region of the checkerboard to better show the illuminated reflective squares, but can significantly increase the noise in the intensity profile. While this technique seemed promising in theory, this turned out to be too imprecise to give accurate results. It is too susceptible to the exposure of the image, and the beam spread due to the water in the tank that must also be taken into account. The tank, being filtered to $0.1 \mu m$

creates a scattering regime, which while small, is still significant and needs to be accounted for beyond just the scattering from water. This scattering and water attenuation has an impact on each of the target positions, requiring compensation to the exposure settings. This needs to be accounted for to obtain accurate results. This technique can only apply to a largely expanded beam or at a large enough distance to get measurable beam spreading. In the future, a higher dynamic range monochromatic camera should be used for this type of experiment.

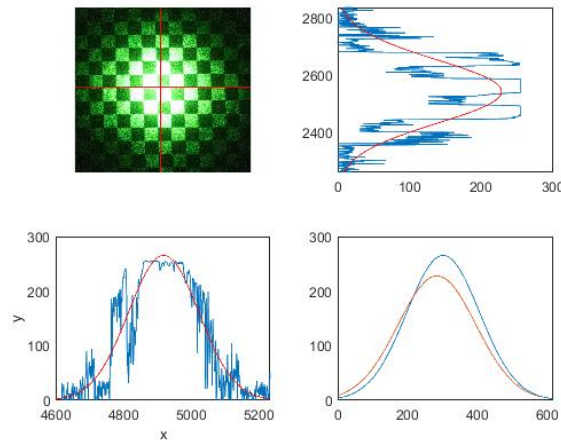


Figure 3.9: Example plot of underwater field of view determination.

3.3.3 SN2 Above Water Field of View Measurement

Ultimately the field of view of SN02 was measured using an external laser aimed with two mirrors and a reflective target. The subsequent signal provided from these measurements was a 2D grid of intensities. Figure 3.10 shows the intensity profile collected at one of the two positions in two views, *i* shows the contour view and *ii* shows a 3-dimensional view. It is apparent from the contour view that the signal is mostly circular. The difference in shape between each side is due to the target not being Lambertian. The positive x direction of *i* is the same side the external laser was on, making its reflectance a more discrete point on the reflector, due to the elongation of the point based on geometry

on the negative side. This effect is visible on the peak intensity, which shows a relative maxima towards the laser position, as well as on the overall shape of the intensity profile. This supported the assumption that the response of the telescope was Gaussian.

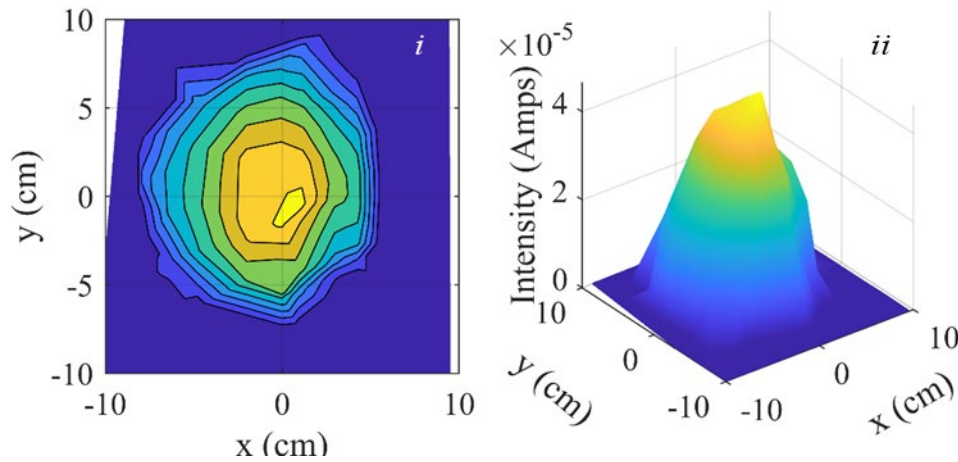


Figure 3.10: Intensity profiles at reflector at 246.7 cm from the exit window.

Vectors were created from the focal point of the unit to the intensity profile positions at each of the positions. Equation 3.3 was then applied to impart the refractive index change onto the vectors. This allowed for two things: an ultimate calculation of the field of view, and calculation of the spot size on the input window. To minimize errors due to the shape of the intensity profile, a 2D Gaussian distribution was fit to the results. The adjusted r^2 value for the fit was 0.95. Ultimately, the two FWHM from the two standoff distances were used to calculate a field of view of 0.0175 radian angle full width. This concurs with initial measurements made and the proposed design of the system.

Using the position of the source laser of SN2 on the reflective target and the field of view at both positions it was confirmed the main axis of the telescope and the main axis of the laser were parallel.

3.3.4 Above Water Beam Characterization

The Beamage camera provided the most consistent results for beam divergence where the laser in question fits within the sensors profile. The camera measures an intensity profile as a function of pixel (distance). The camera software automatically fits a Gaussian to the laser intensity profile. Exporting the profile and taking into account the distance from the exit window provides a measurement of the width of the beam spatially as it moves away from the unit. Table 3.1 shows the full angle results from SN01 and SN02 in two axes. While neither beam was entirely circular, for modeling purposes the average between the two axis was used, providing a half angle divergence of 0.0135 and 0.00235 rad for SN1 and SN2 respectively.

Table 3.1: Green beam divergence results for both systems

	SN1 Angle	SN2 Angle
	(rad)	(rad)
y axis	0.014	0.0057
x axis	0.013	0.0037

3.3.5 SN2 PMT characterization

Due to the relatively low voltages required to produce irradiances which are not oversaturating the PMT sensors, a test was conducted to see if the irradiance of a constant target and geometry are consistent across the PMT voltages used. The results of this test showed that the irradiance was relatively stable across these PMT voltages. Looking at the consistency between scans, 325-500V produces a standard deviation of 0.00055 while 325-550 produces a standard deviation of 0.0028. The ranges used for all scans were between 325 and 500.

3.4 Conclusions

Each component in SN1 was independently characterized while the unit was being built. For SN2 the system was built using the characterization for each of the components in SN1. This component approach required validation after assembly to support the more comprehensive modeling approaches proposed with the second unit. The premeasured values for the field of view were accurate between the two systems. Further characterization was used to both ensure consistency between the two systems, but also to determine a correction to malformations seen in the lidar signals.

More characterization of the electrical impulse response should have been conducted at this point. There was no radiometric calibration conducted on either lidar system. Malformation in the form of inconsistent slopes in homogenous tank tests for both systems was observed. This is more severe for SN2 than SN1, however, this indicates that there is still an error in the electro-optical characterization of both systems. Further work must hunt down the cause of these errors and corrections be formulated and applied to allow accurate inversion. The slope method is uniquely susceptible to such malformations and without a true accounting of the system characterization it is questionable whether the slope method is a viable method with these two lidars. A spatio-angular relationship is assumed to be the culprit and must be explored to correct any data taken with these two systems.

4 Tank, Model and Field Results of two Lidar System

4.1 Introduction

Tank tests allow for a controlled environment in which to test lidar systems. With the inclusion of modeling this controlled environment allows for vigorous validation of the model results. In this experiment both lidar systems (SN1 and SN2) were put into the tank with suspensions of AZRD and BaSO₄. Attempts to validate the model with these results had mixed results. Malformations in the measured waveforms, likely caused by a poor understanding of the characteristics of the lidar lead to questionable inversions. The two lidar systems are slightly different in their geometries, but do exhibit this same malformation. Even so the results of measured and modelled backscatter waveform highlight where more work is required to get proper lidar signal inversion.

Field tests were conducted with only SN2. Field tests can act as a test bed to look at the real-world variability in inversion techniques. Widespread use of the sensors also aides in producing robust inversion techniques. Here field data is presented, however, the same malformation in the lidar waveform highlights the work yet to do to tease out the lidar system response and the IOPs of interest.

4.2 Methods and Materials

4.2.1 Tank experiments

The HBOI Ocean Visibility and Optics Laboratory is a blacked out building housing two lidar test ranges. The range used here is a tank measuring 6.5x12.5x2 meters.

Approximately 60,000 black 2 inch spheres are placed on the surface of the tank to add to the light rejection as well as to limit specular reflections from the air-water interface. The black spheres are 99% effective at light rejection. There are a bank of filtered jets on three of the four corners of the tank. The filters remove particles above $1\ \mu\text{m}$. The jets can introduce both filtered and unfiltered water at three height levels within the tank. This aids in controlling and homogenizing the particle population within the tank. In preparation for using the tank coagulants can be employed to aid in removal of residual particles after filtering. This was not done except before large efforts. Most tank tests occur in the span of 1-2 days. The tank is prepared by filtering the water for a minimum of 36 hours after the introduction of the spheres, and the system is further run for an additional 24 hours with the filters out of line before adding particles. These preparations were used to aid in removing any particles that would be resuspended from the tank or shed from the spheres.

Two test particles were used in tank tests: Arizona Road Test Dust (AZRD) and Barium Sulfate (BaSO_4). AZRD and BaSO_4 are both scattering particles with high albedos of 0.85 and 0.98 respectively. With this lack of absorption, they are a perfect medium to test a lidar that measures backscattered light. The concentration of particles was systematically controlled to increase attenuation in known steps nominally $0.1\ \text{m}^{-1}$ from a filtered tank to roughly $1.2\ \text{m}^{-1}$. Barium Sulfate has a propensity for aggregation requiring that a surfactant, Sodium Hexametaphosphate, be included in the Barium Sulfate suspensions. Particles were mixed with tank water and released in front of jets on one corner of the tank. At least a half an hour was allowed for complete mixing between additions of particles.

4.2.2 Lidar Measurement

The lidar was pole mounted at one end of the tank at a midwater depth. A dark absorbing curtain was used to cover the other end of the tank to create a homogenous surface. This also removed specular scattering from windows on the far end of the tank. 10,000 waveforms were collected for each particle addition.

4.2.3 SN1 Slope Calculation

Waveforms were range corrected and the natural logarithm applied in accordance with equation 2. Waveform slopes were calculated by detecting linear regions of the waveforms using the first and second derivative. The geometric common volume is used as a discriminator between the beginning of the measurable region.

4.2.4 Tank measurements

Tank measurements of both AZRD and BaSO₄ were conducted following the conditions set out in section 1. Extra additions were included in the Barium Sulfate test to allow for larger attenuation resolution for SN2 than SN1. The AZRD and tank tests and BaSO₄ tank test for SN1 were conducted in less than 24 hours, where the added resolution on the SN2 BaSO₄ test required 36 hours over two days.

4.2.5 IOP Measurement

For all tank tests, at least one WET Labs ac-9 was used to provide absorption and attenuation. Standard temperature and salinity corrections were conducted using data from an SBE 37 following Twardowski (1999). The scattering correction applied was the PROP-RR method (Stockley et al. 2017). This method includes the real absorption beyond 700nm typically removed by other scattering methods, providing more accurate absorptions. Phase

functions were measured from 10 to 170 degrees at 10 degree increments using the Multi-Angle Scattering Optical Tool (MASCOT). These measured volume scattering functions were then compared with Fournier-Forand phase functions in order to produce full phase functions between zero and 180 degrees. Water phase functions and scattering were included using the method laid out by Zhang (Zhang, Hu, and He 2009).

Including the MASCOT also allowed for the detection of a small particle population at the beginning of tests below $1\mu m$. This small particle scattering was added into the phase functions to increase accuracy in this model input. Another deviation was a correction to the ac9 attenuation measurement. The ac-9 and ac-s instruments have a non-idealized collector which has an acceptance angle of 0.93° allowing for scattering to influence the absorption measurement. This necessitates a correction using the near forward volume scattering function to remove some of the signal which is scattered at small angles and is counted against attenuation. This is accomplished using:

$$c_p = \frac{\int_0^{0.93} \beta \sin(\theta)}{\int_0^{180} \beta \sin(\theta)} c_{p-uncorrected} \quad (4-1)$$

Where $\beta(\theta)$ is the volume scattering function, c_p and $c_{p-uncorrected}$ are the scattering corrected and uncorrected attenuation respectively.

4.2.6 SN2 Field Data

Field data was collected at Fort Lauderdale, FL (USA) over two days (4/23/2019 and 4/24/2019) out of the Florida Atlantic University SeaTech campus. The boat was driven to deep low c water and was then allowed to slowly move into shore by wind and tides. A lidar and IOP frame were used to measure the optical properties of the water. The lidar was on a pole mount at approximately 1 meter depth. The IOP frame measured in

three scan types: downcasts (dn), upcasts (up) and timeseries (ts). Down and up casts were conducted at approximately 0.1 m/s with frequent stops at depths of interest during deployment. Time series scans were conducted with the IOP frame between 2 and 5 meters deep. The IOP frame was fitted with the standard set of instruments including an ac9 and MASCOT.

Fifty-eight lidar scans were collected simultaneously with the IOP frame while the boat was underway. To match up the data time synchronization was conducted between the two systems. All data was binned to 1 Hz, and matched with GPS information. This data was then split into the three deployment methods for the IOP frame. For down and up casts the data was restricted to between 1 and 10 meters deep. Both timeseries and down and up casts were matched with lidar scans and their respective K_{sys} as calculated by Equation 1.5. Outliers in both datasets were removed using *rmoutliers* with a +/- 2.5 standard deviation limit. Attenuation data and K_{sys} data was averaged for each distinct site/cast type in order to view the data in a meaningful way.

4.2.7 SN2 Digitizer timing correction

To correct for timing discrepancies between waveforms for SN2 the *finddelay* function in Matlab was used. *finddelay* uses cross-correlation between each pair of signals to determine the difference in timing. The delay is calculated as the negative of the lag for the cross-correlation which has the largest absolute value.

4.2.8 SN2 Outlier Scan Removal

After correcting for timing, erroneous scans need to be removed. Three criteria were set for each set of scans to remove erroneous scans if: (1) the position of the maximum intensity is greater than 15 cm apart from the average, (2) the intensity across the first 100

time bins has greater than 10% of its values falling greater than 2.5 standard deviations from the mean, and (3) the maximum intensity is more than 2.5 standard deviations from the mean.

4.3 Results

4.3.1 *SN1 Tank and Model Results*

For the measured BaSO₄ and AZRD waveforms there was a slight increase of the lidar slope for the 2-4 m region. This effect increased as the turbidity of the tank was increased. This suggests that the particle population within the tank was either heterogeneous during measurement or poor characterization is leading to effective changes in lidar sensitivity with distance. The measured lidar returns had significantly greater slopes than the simulated returns at low turbidities. Figure 4.1 shows two examples of model (black line) and simulation (red dotted line) for a low and high attenuation, *i* and *ii* respectively.

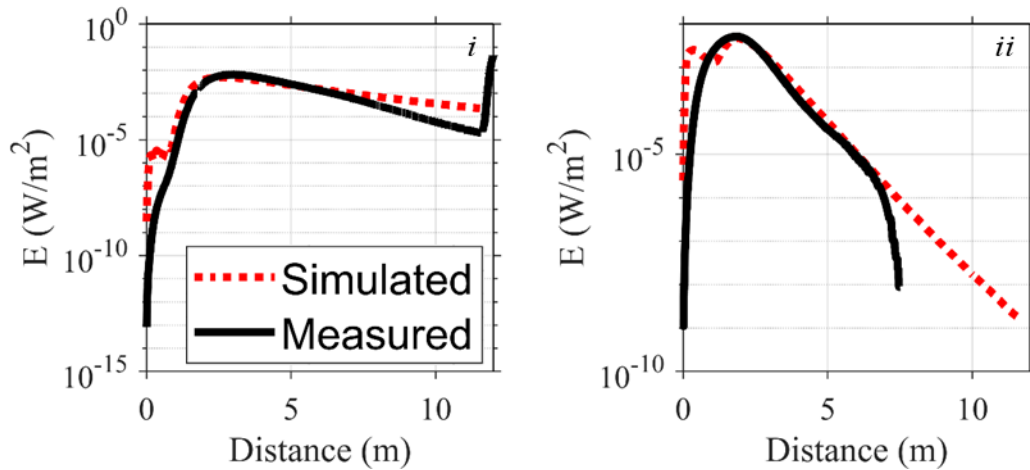


Figure 4.1: Example BaSO₄ measured (black) and simulated (red) matchups for c 532 nm (i) 0.1 m^{-1} and (ii) 1 m^{-1} .

At higher turbidities, the measured and simulated K_{sys} were approaching the same value for 473 nm. For 532 nm there was a consistent positive offset between the simulated and measured slopes. In all measured cases the slope of the lidar return was larger than c (Figure 4.2).

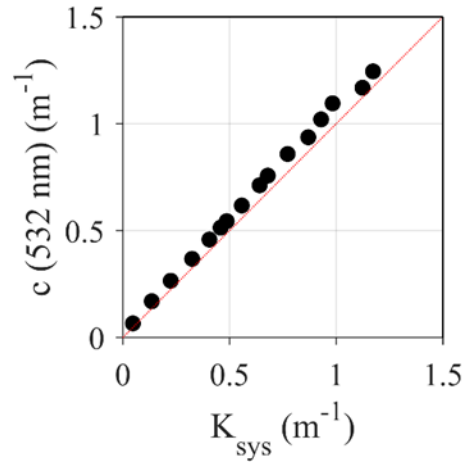


Figure 4.2: Relationship between measured attenuation with ac-9 and range corrected lidar slope, i.e., K_{sys} , of simulated waveforms at 532 nm for $BaSO_4$.

Simulations of the barium sulfate suggest the SN1 K_{sys} values, at low c values and at 532 nm, trend linearly with c . The slopes of the two plots of c vs K_{sys} were 1.02 and 1.4 for 532 and 473 nm, respectively.

The AZRD scans had similar results where the K_{sys} was also found to be higher than measured c for clear waters. As the turbidity increased however, the system tended towards a and K_d rather than towards c , with $\frac{K_{sys}}{c}$ values averaging about 0.3. AZRD has a single scattering albedo of 0.85 on average at 532 nm. Even with this high albedo it still behaves quite differently than the $BaSO_4$. The system specific lidar slope did follow a linear relationship for this set of data as well.

Figure 4.3 shows the short-range determination of attenuation at 532 using the ratio of multiple scattered energy to the common volume energy for the simulated waveforms for barium sulfate. The form of the fit is a 3-parameter exponential equation ($y = y_0 + a \cdot \exp(b \cdot x)$). Each wavelength did have a small intercept offset: 0.077 and 0.040 for 532 and 473 nm respectively and the a and b values are 0.062 and 4.04 for 532 and 0.071 and 4.01 for 473 nm.

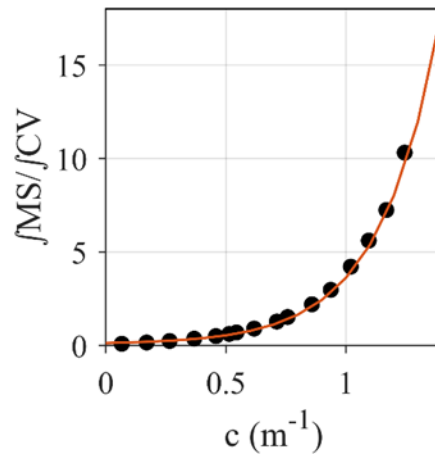


Figure 4.3: Ratio of the integral of the multiple scattering signal and the integral of the common volume.

4.3.2 SN2 Lidar Tank, Model and Field Data

Attenuations for the two SN2 tank tests vs. their addition numbers are shown in figure 4.4. There were 12 and 29 additions of test particles for AZRD and BaSO₄ respectively. The dip in BaSO₄ attenuation is due to the experiment taking roughly 36 hours distributed over two days. The tank was not allowed to filter, but the loss in attenuation was due to settling and coagulation of barium sulfate overnight. Even with the inclusion of Sodium Hexametaphosphate, the rate of removal is quite high with these large particles. The AZRD test saw a max c of 1.2 while the BaSO₄ saw a max c of 1.3. Both particles have high albedos, 0.88 and 0.98 AZRD and BaSO₄ respectively, which approach their max as c increases. Above 0.5 m^{-1} both have albedos above 0.8.

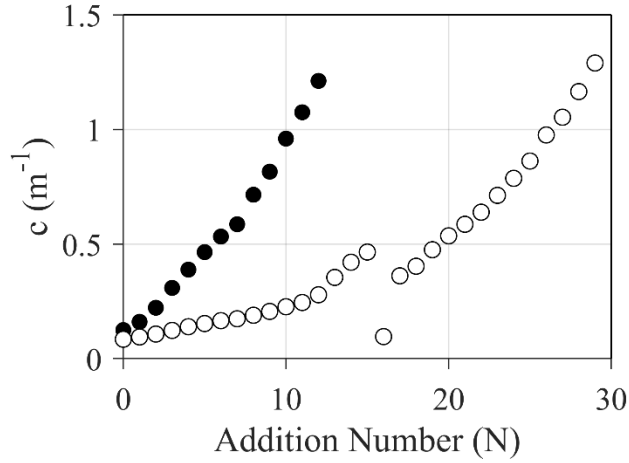


Figure 4.4: AZRD and Barium Sulfate addition numbers vs attenuation. Closed circles are AZRD and open circles are Barium Sulfate.

The timing between waveforms is controlled via the photocathode which determines when the PMT should be triggered to begin a scan. However, if the digitizer inaccurately accounts for the time between triggers, it leads to changes in the position of a hard return or even the common volume position. Errors due to digitizer timing can be seen as deviations between the times of flight to a target in waveforms (Figure 4.5). While the timing is consistent within a waveform the error occurs in the timing between scans. It was observed that such an error broadens and decreases the magnitude of features. It was found that the distance to a target oscillated with an accuracy of ± 0.5 meters, roughly 10 time bins.

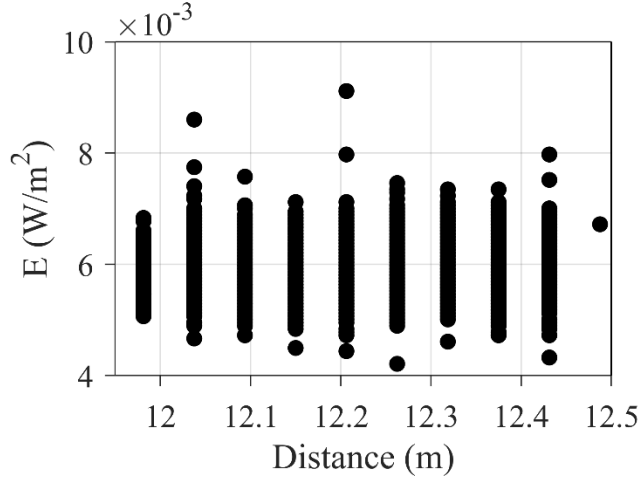


Figure 4.5: Example of hard target return highlighting digitizer timing jitter

For low turbidities where the backscattering from the back of the tank or a target is distinct, timing correction is as simple as matching the timing of the peak of the hard return for all waveforms in the average. However at higher turbidities, or where there is no hard return, this method becomes impossible due to lack of sufficient signal return. Attempts to correct without a target lead to a process of searching for common features in waveforms to correct the timing between them. Low pass filtering was employed to help remove noise from the backscattered return. Derivative analysis was used to determine points of congruity between waveforms. This was not fruitful. Low pass filtering removed and broadened features of interest, intrinsically changing the shape of the average waveform. It was for this reason that the signal processing function *finddelay* was employed. The delay was quantified between each scan, and finally the delay was determined between the average corrected scans and the mean scan. It is assumed in this method the mean delay holds the appropriate timing. This greatly reduced the standard deviation between waveform averages. This also aided in removing some ambiguity in the comparisons between modeled and measured results. Figure 4.6 shows the difference in timing for

corrected and uncorrected waveform averages. The broadening of the second peak (hard target return) highlights the affect the timing jitter imparts on the average waveform. Outlier scan removal was also conducted following the criteria outlined in the methods. Nearly no removal occurred due to the first criteria (offset max value). Most of the removals are due to the third criteria, typically making up more than 50% of the total removals. Of the typical 10,000 scans, the maximum removed from any measurement was 1997 scans with the majority removing less than 10%. Removals decreased with higher signals. Using the mean and outlier removal showed superior performance over a low pass filter and preserved features within the waveform more accurately.

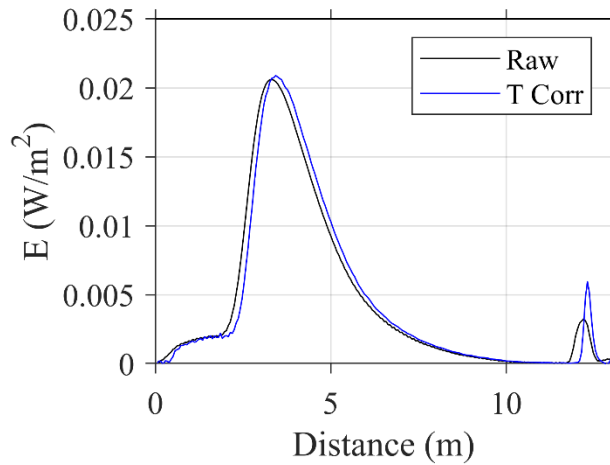


Figure 4.6: Average of scans before (black) and after (blue) timing correction, showing broadening of signal due to distance uncertainties.

A significant issue present in both lidars is that in moderate to high c , the far field of scans shows an increase in returned light with distance. Figure 4.9 is an example of the elevation seen in the far field in high turbidity measurements. This is assumed to be due to a shift in the distribution of light on the PMT surface with distance and c . “Eclipsing” and “burning” of photons on the PMT are suspected to be the culprits as the angular acceptance of photons changes the distribution of photons across the PMT surface in the far field. By

not focusing across the entirety of the PMT surface, the response will vary spatially. This violates assumptions of the slope method. An attempt to create an overlap correction function taking into account the geometric and radiometric properties of the PMT “eclipsing” and “burning” requires more investigation. Furthermore, a simple physical correction using a diffuser before the PMT after the bandpass filters has also been proposed. This may be pursued in the future.

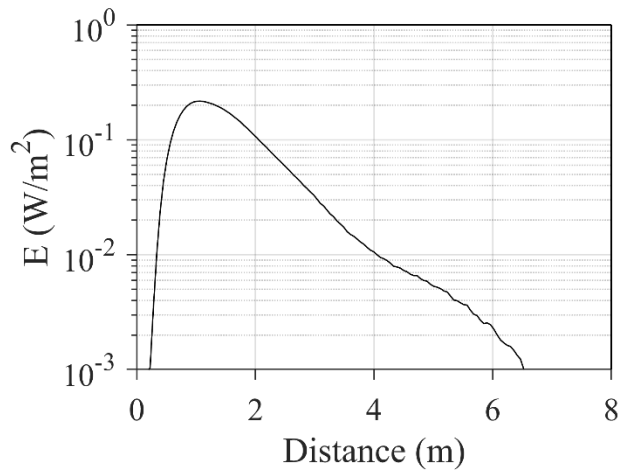


Figure 4.7: Example enhancement at higher c scan (0.97 m^{-1}) showing enhancement after 4 meters.

4.3.2.1 SN2 Model Validation

The Metron model provides decent performance in producing backscattered waveforms given the conditions within the tank. While comparisons of shape showed consistency, the magnitudes of the waveforms were not comparable. While this was an issue it has been deemed inconsequential for the use of the slope method, as the primary concern is the shape and not the magnitude of the backscattered return waveforms. For this reason, both the simulated and measured datasets are normalized to the total energy between 1 and 5 meters.

Many sensitivity runs were made to both better understand model responses to changes in input parameters and to determine if the enhancement could be explained using inputs to the model. A set of 16 model runs were selected where individual parameters were changed independent of the others. Three distinct groups of changes were made to the dataset to determine their impact on the model results. The three categories were (1) changes to the phase function, including changes to the near forward and backscattering components of the phase function, (2) changes to IOPs including a and c , and (3) changes to the scaled pulse laser characterization input to the model. In all cases, improved performance was not seen between any sensitivities when compared to the measured data. There was never a situation where this enhancement could be modeled. Because the model assumes an idealized detector system the enhancement seen was never likely to be modeled using the Metron code. Another test was changing the shape of the receiver from Gaussian to uniform circular. This change resulted in improved waveform shape. It was later found that this version of the model did not accept the Gaussian shape as an input, although it is an option. Switching off Gaussian led to the greatest improvement in performance.

Metron fits were best for middle attenuations for both AZRD and BaSO₄. An example of fits between measured and modelled waveforms for three attenuations are shown in figure 15. Attenuation was 0.085, 0.816 and 1.29 m⁻¹ for *i*, *ii* and *iii* respectively. The matches in the middle of the three examples show how the resulting modeled slopes were more impacted by attenuation than the slopes from the measured data. Improved matches in mid-range c waveforms is likely serendipitous, as the measured data slope shows a lower sensitivity to c than the modelled results. Differences in the shape of the multiple scattering and common volume regions are also points of interest for future work.

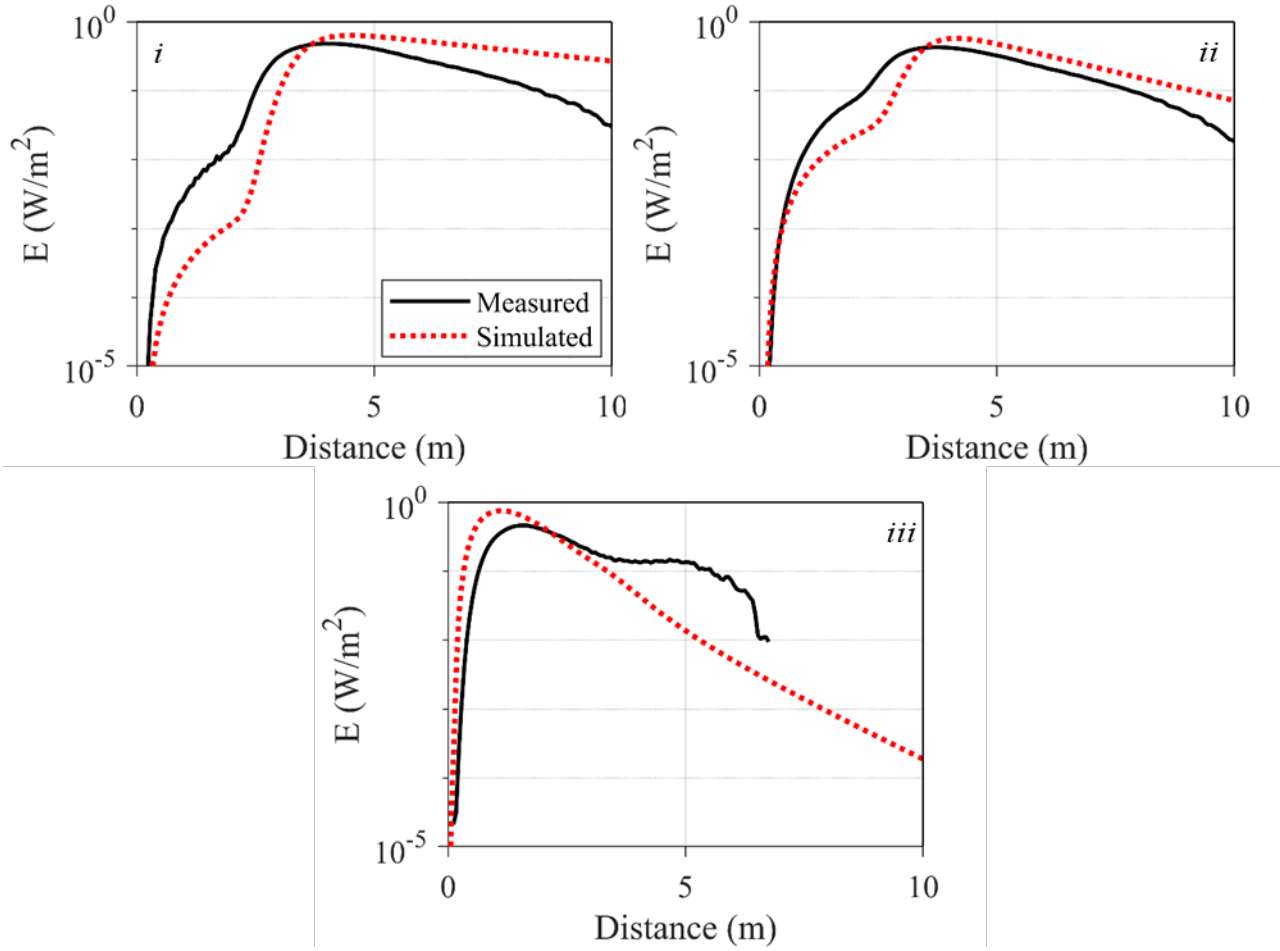


Figure 4.8: Examples of Metron simulations and measured data fits for three attenuations 0.085, 0.816 and 1.29 m^{-1} for i, ii and iii respectively.

Figure 4.9 shows the relationship between c and K_{sys} for the measured tank dataset. The AZRD and BaSO_4 tests had very similar relationships. AZRD predicted $K_{sys} = 0.09 * c(532) + 0.173$ and BaSO_4 was $K_{sys} = 0.171 * c(532) + 0.118$. This is heartening since the differences in these two particle types, one synthetic and the other natural, suggests that the lidar performs similarly across many different particle assemblages. However, the relationship between c and K_{sys} show that the system does not show a strong change in waveform slope due to the attenuation, especially at higher c .

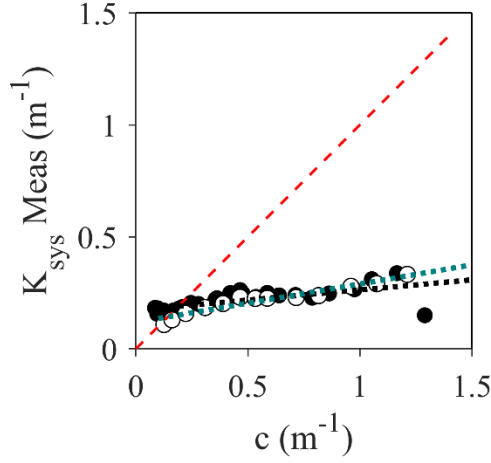


Figure 4.9: c vs K_{sys} for measured tank data. Open circles and green line are $BaSO_4$ and closed circles with black line are AZRD.

The K_{sys} calculated from simulated waveforms showed a relationship between c and K_{sys} which is more typical to lidar systems. Figure 4.10 shows a characteristic “roll off” in K_{sys} sensitivity as c increases.

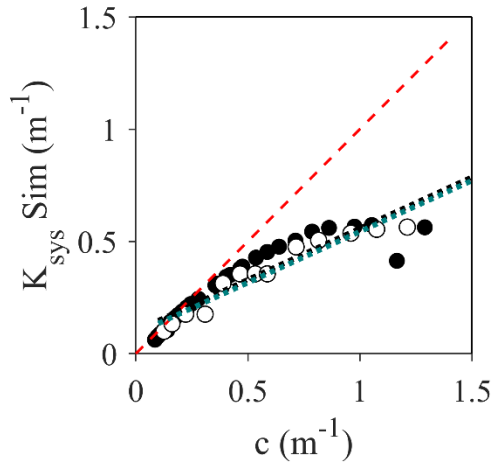


Figure 4.10: c vs K_{sys} for simulated tank data. Open circles and green line are $BaSO_4$ and closed circles with black line are AZRD.

The difference between the measured and simulated slopes do show a relatively strong linear relationship, however as seen in Figure 4.8 this may be somewhat spurious. Figure 4.11 shows the relationship between the measured and simulated slope values. The

simulated K_{sys} was roughly 2.5 times larger than the K_{sys} measured with a significant negative offset (-0.19). The difference between the simulated and measured slopes is likely due to the enhancement seen at higher turbidities in the far field. The idealized impulse response of the simulated dataset is incapable of predicting this shape.

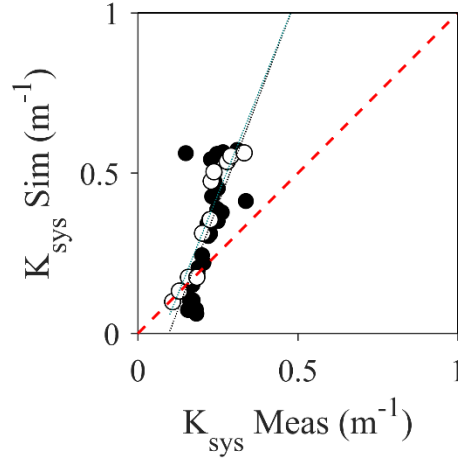


Figure 4.11: Comparison of K_{sys} calculated from both measured and simulated data for $BaSO_4$ and AZRD.

4.3.2.2 SN2 Field Data

The sampling area off Fort Lauderdale Florida (USA) is presented in Figure 4.12. The lines indicate the paths taken on the two days of sampling 4/23 and 4/24, 2019 for green and red respectively.

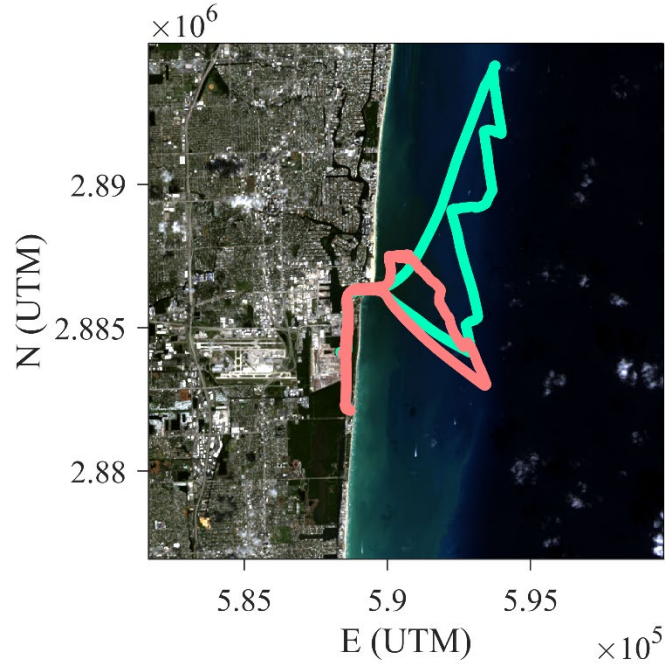


Figure 4.12: Map of Fort Lauderdale test track, the green and red lines are the tracks for 4/23/2019 and 4/24/2019 respectively.

Figure 4.13 shows the 1 Hz binned attenuation dataset from all of the sites and casts. The in harbor sites were the only values greater than 0.5 m^{-1} (shown in red) with values averaging at 1.8 m^{-1} . This data was collected in a turn basin after resuspension from a recent turning ship. Here, multiple angles of the pole mount were measured, however any water column inhomogeneity was not detectable to the lidar.

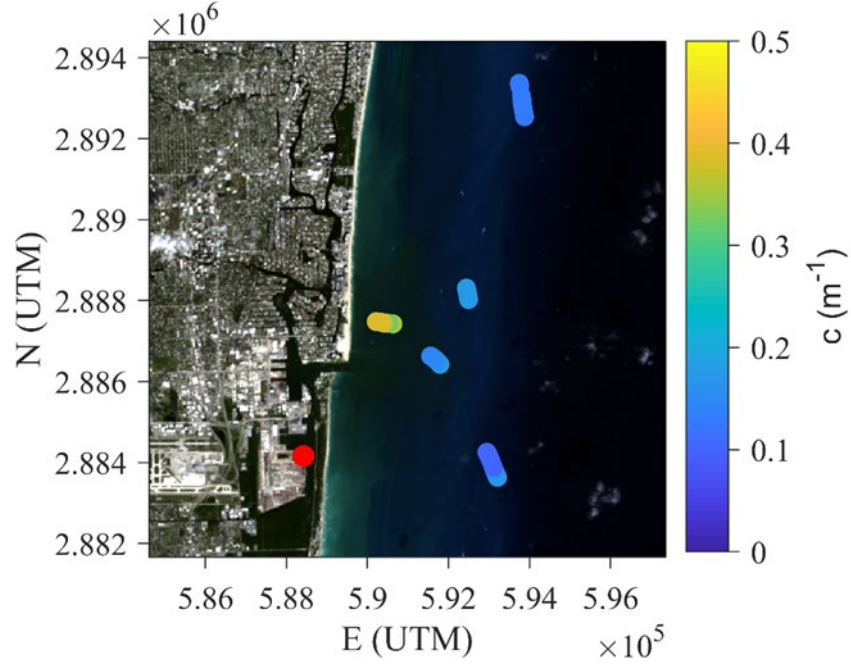


Figure 4.13: Distribution of c values for Fort Lauderdale sampling sites. Only data where there is both lidar and IOPs are shown.

Figure 4.14 shows 1 Hz binned lidar waveforms. It is easy to see that there are some features detected and differences in slopes through the duration of the scan. The ac-9 measurements of attenuation were slowly decreasing through this measurement from a maximum of 0.28 to 0.21 m^{-1} . Variations in the surface water are most likely from the ships motion into shore. There were observable changes in water attenuation as the ship travelled closer to shore. One shortcoming of an ac-9 versus the lidar is apparent as small fluctuations in attenuation as measured by the lidar are not necessarily detected by the small sampling volume of the IOP instrumentation. This restricted the analysis to using an average water column c when comparing attenuation and K_{sys} .

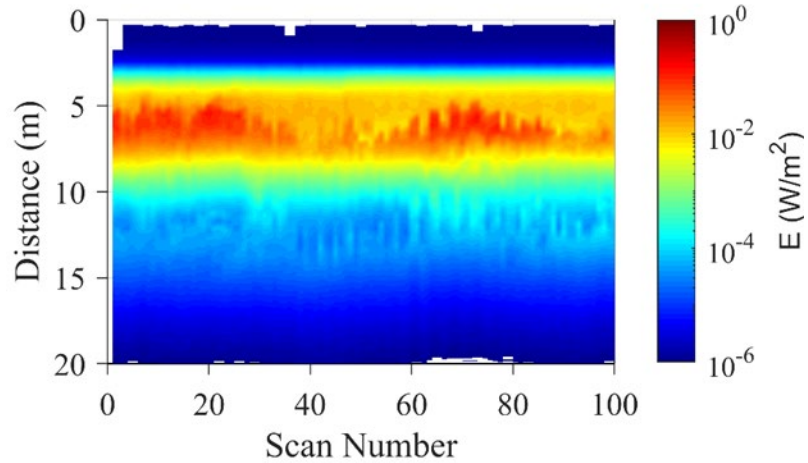


Figure 4.14: Example scans in deep water from 4/23/2019 at 11:01 with PMT at 475V.

Figure 4.15 shows an example of a mid-range attenuation water with moderate c . Here the average c value was 0.37 m^{-1} , with c towards the end of the scan reaching as high as 0.442. A midwater plume is observable across the entirety of the scan. This again highlights the benefit of using lidar traditional profiling instrumentation. These features were not observable in the IOP dataset. The lidar can measure a much larger volume instantaneously while some of these features are lost in the IOP data. A methodology like a modified Klett (Evans 1984) would be beneficial to attempt to measure instantaneous c at each depth along the waveform. This methodology is, however not strongly explored here or in the literature outside of atmospheric research.

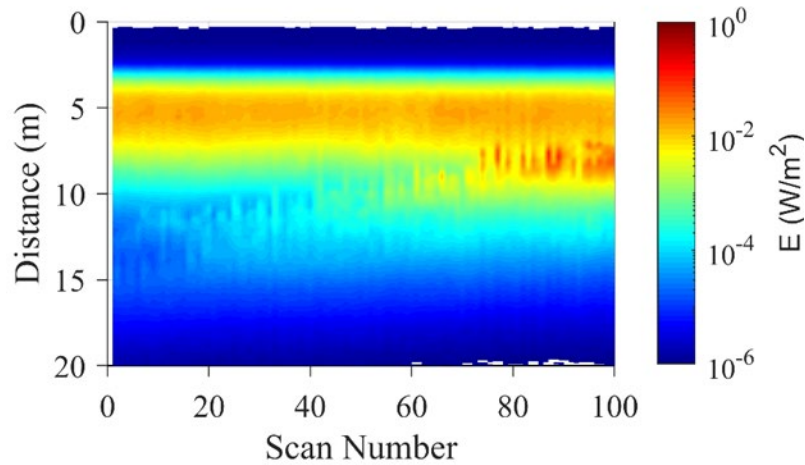


Figure 4.15: Example plot in deep water showing a scan from 4/23/19 at 10:59 with PMT at 475V.

Figure 4.16 shows a transect where the lidar was set in shallow water as the boat travelled. A strong bottom signature is visible in these waveforms as a large return around 7 meters. The average water column attenuation was 0.41 m^{-1} . One benefit seen here is the lidars ability to measure at thin layers and around boundaries. There is data available right up to the boundary along the sediment sea-interface. These zones can be dynamic and important to understand the properties of the water column including nutrient and sediment transport. These regions typically require specialized equipment or cruises to be measured, or else risk grounding and damaging existing systems.

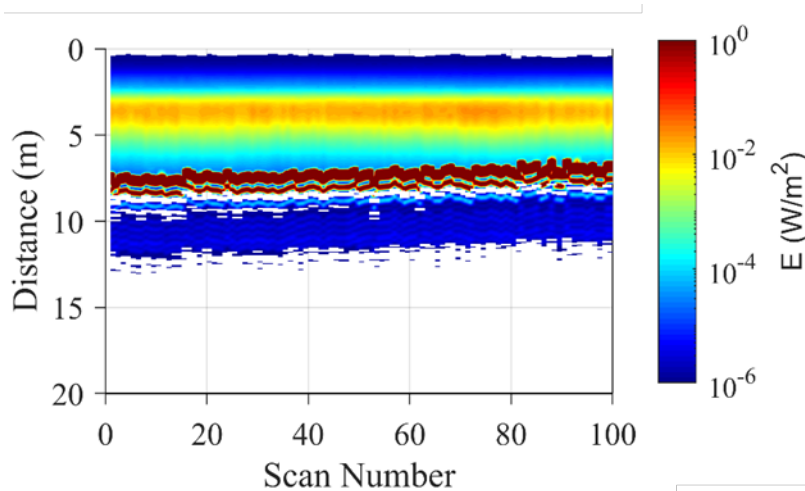


Figure 4.16: Example plot in shallow water showing a scan at 11:43 4/24/19 at PMT at 425V.

Figure 4.17 shows the average K_{sys} and c values for all casts from the Fort Lauderdale, FL (USA) field effort. Individual matchups were averaged along casts in order to better account for changes in c without the influence of depth or cast type. For this reason some variation is lost for both the lidar and IOP measurements. This highlights the need for inversion techniques to allow for each instrument to work independently. For these values, there was good 1:1 closure between the measured IOPs and calculated K_{sys} for low c waters. At higher attenuations there is a predictable roll-off in the slope methods sensitivity. This is most likely due to multiple scattering dominating the signal. The slope method is based on the single scattering interpretation of lidar signals. With dominance of multiple scattering, the lidar backscatter return is saturated with photons which have undergone multiple interactions essentially allowing photons which have exited the receiver path to reenter the path and be measured. This generates an asymptotic response as attenuation increases.

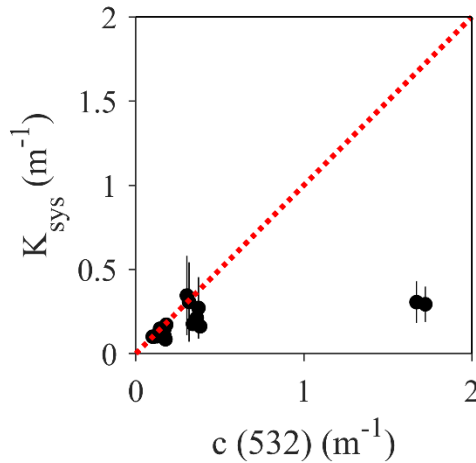


Figure 4.17: c vs K_{sys} for averaged water column attenuations for field dataset. .

Figure 4.18 shows the modified Gordon plot for the field data. There were no values measured between 0.5 and 1.8 m^{-1} . Binning the dataset based on single scatter albedo did show a decent relationship, however without the interceding points between 0.5 and 1.8 m^{-1} , the high values placed undue relevance to the relationship and it is therefore not shown here.

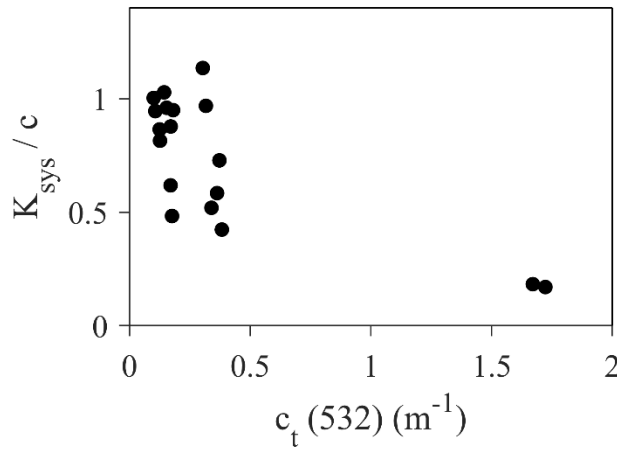


Figure 4.18: Modified Gordon plot for Fort Lauderdale dataset.

4.4 Conclusions

Drawbacks of using the slope method lie with its sensitivity to small changes in homogeneity, systems characterization, and the signal to noise ratio. This basic method does not account for multiple scattering and therefore may have artificially low signals for scattering dominated waters. In the future, several other inversion techniques must be tested incorporating SN1 and SN2 architecture.

SN1 and SN2 were designed to be very sensitive to small changes in light so that it can best detect layers. Calibration methods to account for the specific receiver properties of these lidars are paramount to quantitative analysis and interpretation of data. Inconsistency in performance of theses and significant artifacts present in measured

waveforms were not fully realized until after the experiments were carried out. Much of the literature focuses around systems which have a source receiver separation that is negligible compared to the altitude above the surface of the water which gives an almost complete overlap over the water. This system does have a narrow separation between the telescopes and the source, but this cannot be assumed to be negligible as it is for aerial and satellite borne lidar systems due to the relatively short distance over which the lidar source and receivers overlap. All these parameters can also be explored at both wavelengths of the system. The ideal wavelength for open waters is somewhere between 470 and 490 nm according to Gray et al. (2015). They also determined the green wavelength is useful for moderately turbid waters.

The increased resolution in c for Barium sulfate within the tank tests for SN2 did help to highlight the onset of the far field enhancement. It will eventually be a help in determining an appropriate correction function for SN2. With the elevation in the far field of the waveform the usable range over which slopes can be calculated is truncated. This coupled with uncertainty about this elevation on the remainder of the waveform makes the accuracy of the results for both systems and all turbidities unclear. The success of SN1 in measuring c does indicate that this architecture can be successful, but without appropriate corrections, calibrations and characterizations the system is not providing expected results. The modeling effort highlights, also, that the system should be capable of measuring c with a higher accuracy than is currently presented.

The enhancement in the far field of the waveforms is present in both the tank and field data pointing to it being a systemic error within the system. Understanding the enhancement is required to increase the accuracy of the system. After correction of the

enhancement a determination of how to achieve better validation between the lidar system and the model is required, looking at both the shape and magnitude characteristics of each.

Further tests and analysis with working 473 nm lasers is also necessary to show the errors in the system. Unfortunately, the 473 nm laser failed before many of the tests and was therefore considered virtually unusable for this analysis. Having both $c(532)$ and $c(473)$ would reduce the number of unknowns in the lidar equation as backscattering and the slope of c are valuable to inversion.

An examination of the off axis dataset is also an important part of this experiment that was not completed. The off-axis provides a good measurement of the multiple scattering, presenting information on the shape of the phase function and potential corrections for both range correction and inversion.

An expansion in the number of field measurements between 0.5 and 1.8 m^{-1} would also aid in future inversion attempts. An approach where the IOP profiler is quickly towed through the water column should be conducted to aid in understanding distribution of c values the lidar is observing. By staying in one place and switching between dynamic and homogeneous water columns would provide a perfect test bed for inversion of range gated information.

Future attempts to look at thin layers, and density discontinuities would also help to further characterize the system. As it stands, the majority of the measurements made with this system also target highly scattering waters, where looking into absorbing (lower ω_o) waters would also aid in production of appropriate inversion algorithms. The attenuation and backscattering in the lidar equation do not covary, and a view into these

parameters as one changes while keeping the other constant would lead to better insight into the inversion.

Conclusion and future work

Lidar has great potential to supersede profiling optical technologies available today. However, the confounding effects that system characteristics have on the overall performance of lidar for IOP retrieval cannot be overstated. This problem will continue to exist until appropriate methods exist to isolate the system specific parameters from the backscattered lidar signal.

Unfortunately, due to the small size of the two systems, and the resources allocated to the development of each, the time required to fix or change hardware was large. Many issues including failures of lasers and allocation of time to replace, test and rebuild components in the two systems resulted in the two systems being developed almost independently from one another. As a result, this analysis is not as complete as it could have been. Initial indications from 4.3.1 utilizing the first system (SN1) show that this system was much closer to a c meter than SN2. Unfortunately, SN1 failed and was not fixed in time to retake data for this thesis. Furthermore, there was never a period where both lidars were working at the same time. Side by side comparisons between the two systems with the same hardware but different geometries would have highlighted the differences and benefits of both geometries.

The beam reshaping/combining optics used in these systems were too custom and inflexible to accommodate natural changes in and breakdown of lasers. Although the 532 nm DSSP laser used was relatively stable, a filter originally included by the manufacturer

to remove doping light from the output melted after use and would fundamentally change the properties of the beam. In each system, the blue lasers failed regularly, both by outright refusal to continue lasing, and also changes to their mode. Changes in the mode and/or the lasing properties of the doping laser, resulted in changes to the shape of the laser output. These problems necessitated a redesign of the beam combining optics, a process which was too costly both in resources and time to have adequate turn-around. This led to down-time for both systems which lasted months. To replace a laser was ultimately a time consuming and difficult operation, requiring custom combining optics, a complete dismantling of a system and a reassessment of geometry of the lidar. Eventually, this led to an abandonment of the blue laser data altogether for this project as the down-time was too great to continue. A future system should sport more flexible combining optics which could accommodate new lenses and geometries as laser properties change. Good news for the future is that both lasers have seen significant development improvements since their initial use in this system, although replacing them was not possible in this timeframe.

Further examination of this system should include better PMT characterization, a more advanced overlap function correction and better radiometric calibration. The PMT voltages used for most of this work were very low (350-500 V). These may have caused errors as the dynode chain may not have been efficient or consistent in converting photon energy to current. In section 3, a set of scans supports the assumption that the PMTs performed properly in this voltage range, however a true radiometric calibration of the system is needed. The range of PMT voltages was below the manufacturers gain curve, and therefore an extrapolation of this curve was required for conversion to irradiance. Furthermore an investigation into how to ensure the PMT can be used within its natural

range might help to eliminate errors in photon-electron conversion. Improved characterization of the overlap function and sensitivity of these systems is required. These are the most likely culprits for the waveform malformation observed in the measured waveforms. Slope calculations with these systems will remain suspect until a more rigorous accounting of the increased power with distance in homogenous media is corrected.

The forward modelling approach to lidar inversion shows promise. With a more expansive set of tests into the impact of geometry for profiling lidar systems, both the tailoring of newly developed systems to measure the quantities of interest and inversion of existing systems can move forward. Further validation of the model with existing systems will also lead to proper quantification of the errors in existing inversion techniques and development of new techniques.

The Metron model is typically used with low divergence beams for imaging lidars. However, SN1 with a wider beam divergence showed better results in matches between the measured and simulated datasets. This result should be explored more in the future with side by side measurements taken with both systems. The version of the code available was also incapable of fully characterizing the system parameters, adding to the uncertainty of the closure between modelled and measured results. Radiometric calibration of both sets of data is required to more adequately improve confidence in the closure results. With better calibration and a strong definition of the lidar specific portion of the lidar formula the inversion of IOPs is close at hand.

Appendix

Part of this submission can be found in a SPIE conference paper published in 2018. Permission was granted from SPIE on 10/9/2020. Permission is posted on the following page.

The original work can be found here:

Strait, C., Twardowski, M., Dalglish, F., Tonizzo, A. and Vuorenkoski, A., “Development and assessment of lidar modeling to retrieve IOPs,” *Ocean Sensing and Monitoring X* **10631**, W. “Will” Hou and R. A. Arnone, Eds., 243 – 249, SPIE (2018).

Christopher Strait

From: Shannon Engelbrecht <shannone@spie.org>
Sent: Thursday, October 1, 2020 8:48 PM
To: Christopher Strait
Subject: RE: Reprint permission for student thesis

EXTERNAL EMAIL : Exercise caution when responding, opening links, or opening attachments.

Dear Christopher Strait,

Thank you for seeking permission from SPIE to reprint material from our publications. SPIE shares the copyright with you, so as author you retain the right to reproduce your paper in part or in whole.

Publisher's permission is hereby granted under the following conditions:

- (1) the material to be used has appeared in our publication without credit or acknowledgment to another source; and
- (2) you credit the original SPIE publication. Include the authors' names, title of paper, volume title, SPIE volume number, and year of publication in your credit statement.

Please let me know if I may be of any further assistance.

Sincerely,

Shannon Engelbrecht
Conference Programs & Proceedings Assistant
TEL: +1 360 676 3290
shannone@spie.org
SPIE is the international society for optics and photonics
<http://SPIE.org>



References

- Chen, Shuguo, Cheng Xue, Tinglu Zhang, Lianbo Hu, Ge Chen, and Junwu Tang. 2019. "Analysis of the Optimal Wavelength for Oceanographic Lidar at the Global Scale Based on the Inherent Optical Properties of Water." *Remote Sensing* 11 (22): 2705. <https://doi.org/10.3390/rs11222705>.
- Churnside, James H. 2001. "Airborne Lidar for Fisheries Applications." *Optical Engineering* 40 (3): 406. <https://doi.org/10.1117/1.1348000>.
- . 2013. "Review of Profiling Oceanographic Lidar." *Optical Engineering* 53 (5): 051405. <https://doi.org/10.1117/1.OE.53.5.051405>.
- Churnside, James H, and Percy L Donaghay. 2016. "Thin Scattering Layers Observed by Airborne Lidar," 12.
- Churnside, James H., and Richard D. Marchbanks. 2015. "Subsurface Plankton Layers in the Arctic Ocean." *Geophysical Research Letters* 42 (12): 4896–4902. <https://doi.org/10.1002/2015GL064503>.
- Churnside, James H., James M. Sullivan, and Michael S. Twardowski. 2014. "Lidar Extinction-to-Backscatter Ratio of the Ocean." *Optics Express* 22 (15): 18698. <https://doi.org/10.1364/OE.22.018698>.
- Ciotti, Aurea M., and Annick Bricaud. 2006. "Retrievals of a Size Parameter for Phytoplankton and Spectral Light Absorption by Colored Detrital Matter from Water-

Leaving Radiances at SeaWiFS Channels in a Continental Shelf Region off Brazil: Algal Size and CDM from SeaWiFS Data.” *Limnology and Oceanography: Methods* 4 (7): 237–53. <https://doi.org/10.4319/lom.2006.4.237>.

Ciotti, Áurea M., Marlon R. Lewis, and John J. Cullen. 2002. “Assessment of the Relationships between Dominant Cell Size in Natural Phytoplankton Communities and the Spectral Shape of the Absorption Coefficient.” *Limnology and Oceanography* 47 (2): 404–17. <https://doi.org/10.4319/lo.2002.47.2.0404>.

Dalglish, Fraser, Frank Caimi, Yueting Wan, Walter Britton, Joseph J Shirron, Thomas E Giddings, Charles H Mazel, James M Glynn, and Jonathan P Towle. 2008. “Experimental Validation of a Laser Pulse Time-History Model,” 9.

De Wolf, D. 1971. “Electromagnetic Reflection from an Extended Turbulent Medium: Cumulative Forward-Scatter Single-Backscatter Approximation.” *IEEE Transactions on Antennas and Propagation* 19 (2): 254–62. <https://doi.org/10.1109/TAP.1971.1139894>.

Einstein, Albert. 1905. “Concerning an Heuristic Point of View Toward the Emission and Transformation of Light.” *Annalen Der Physik* 4 (17): 135–48.

Evans, B T N. 1984. “On the Inversion of the Lidar Equation.” Unclassified Unlimited Distribution 1/24/1985. Research and Development Branch Department of Natinal Defence Canada.

Feygels, Viktor I., Yuri I. Kopilevich, Alexey I. Surkov, James K. Yungel, and Michael J. Behrenfeld. 2003. “Airborne Lidar System with Variable-Field-of-View

Receiver for Water Optical Properties Measurement.” In , edited by Robert J. Frouin, Gary D. Gilbert, and Delu Pan, 12. <https://doi.org/10.1117/12.506976>.

Fletcher, Robert. 1969. “Meteorological Resources and Capabilities in the ’70’s.” Proceedings of the 5th AWS Technical Exchange Conference Air Force Academy 14-17 July 1969 217. Air Force Academy.

Fournier, Georges R., and J. Luc Forand. 1994. “Analytic Phase Function for Ocean Water.” In *Ocean Optics XII*, 2258:194–201. International Society for Optics and Photonics. <https://doi.org/10.1117/12.190063>.

Giddings, Thomas E., and Joseph J Shirron. 2009. “Numerical Simulation of the Incoherent Electro-Optical Imaging Process in Plane-Stratified Media.” *Optical Engineering* 48 (12): 126001. <https://doi.org/10.1117/1.3274936>.

Gordon, Howard R. 1982. “Interpretation of Airborne Oceanic Lidar: Effects of Multiple Scattering.” *Applied Optics* 21 (16): 2996. <https://doi.org/10.1364/AO.21.002996>.

Gray, Deric J., John Anderson, Jean Nelson, and Jarrod Edwards. 2015. “Using a Multiwavelength LiDAR for Improved Remote Sensing of Natural Waters.” *Applied Optics* 54 (31): F232. <https://doi.org/10.1364/AO.54.00F232>.

Hamamatsu. 2017. *Photomultiplier Tubes: Basics and Applications*. 4th ed. Hamamatsu Photonics K.K. https://www.hamamatsu.com/resources/pdf/etd/PMT_handbook_v4E.pdf.

Hertz, Heinrich. 1887. “Ueber Einen Einfluss Des Ultravioletten Lichtes Auf Die Electriche Entladung.” *Annalen Der Physik* 267 (8).

Hoge, Frank E., Robert Swift, and James Yungel. 1995. "Oceanic Radiance Model Development and Validation: Application of Airborne Active–Passive Ocean Color Spectral Measurements." *Applied Optics* 34 (18): 3468–76. <https://doi.org/10.1364/AO.34.003468>.

Houston, J. D., and A. I. Carswell. 1978. "Four-Component Polarization Measurement of Lidar Atmospheric Scattering." *Applied Optics* 17 (4): 614. <https://doi.org/10.1364/AO.17.000614>.

IOCCG. 2006. "Remote Sensing of Inherent Optical Properties: Fundamentals, Tests of Algorithms and Applications. Lee, Z.-P. (Ed.)." 5. Reports of the International Ocean-Colour Coordinating Group. Dartmouth, Canada. <https://ioccg.org/wp-content/uploads/2015/10/ioccg-report-05.pdf>.

Katsev, Iosif L., Eleonora P. Zege, Alexander S. Prikhach, and Igor N. Polonsky. 1997. "Efficient Technique to Determine Backscattered Light Power for Various Atmospheric and Oceanic Sounding and Imaging Systems." *Journal of the Optical Society of America A* 14 (6): 1338. <https://doi.org/10.1364/JOSAA.14.001338>.

Kattawar, George W., and Gilbert N. Plass. 1972. "Time of Flight Lidar Measurements as an Ocean Probe." *Applied Optics* 11 (3): 662. <https://doi.org/10.1364/AO.11.000662>.

Kim, Hongsuk H. 1973. "New Algae Mapping Technique by the Use of an Airborne Laser Fluorosensor." *Applied Optics* 12 (7): 1454–59. <https://doi.org/10.1364/AO.12.001454>.

Liu, Qun, Xiaoyu Cui, Weibiao Chen, Chong Liu, Jian Bai, Yupeng Zhang, Yudi Zhou, et al. 2019. “A Semianalytic Monte Carlo Radiative Transfer Model for Polarized Oceanic Lidar: Experiment-Based Comparisons and Multiple Scattering Effects Analyses.” *Journal of Quantitative Spectroscopy and Radiative Transfer* 237 (November): 106638. <https://doi.org/10.1016/j.jqsrt.2019.106638>.

Loisel, Hubert, and André Morel. 1998. “Light Scattering and Chlorophyll Concentration in Case 1 Waters: A Reexamination.” *Limnology and Oceanography* 43 (5): 847–58. <https://doi.org/10.4319/lo.1998.43.5.0847>.

Maiman, T. H. 1960. “Stimulated Optical Radiation in Ruby.” *Nature* 187 (4736): 493–94. <https://doi.org/10.1038/187493a0>.

Middleton, W. E. K., and A. F. Spilhaus. 1953. “Meteorological Instruments.” *Quarterly Journal of the Royal Meteorological Society* 80 (345): 484–484. <https://doi.org/10.1002/qj.49708034532>.

Morel, André. 1988. “Optical Modeling of the Upper Ocean in Relation to Its Biogenous Matter Content (Case I Waters).” *Journal of Geophysical Research* 93 (C9): 10749. <https://doi.org/10.1029/JC093iC09p10749>.

———. 2009. “Are the Empirical Relationships Describing the Bio-Optical Properties of Case 1 Waters Consistent and Internally Compatible?” *Journal of Geophysical Research* 114 (C1). <https://doi.org/10.1029/2008JC004803>.

Morel, André, David Antoine, and Bernard Gentili. 2002. “Bidirectional Reflectance of Oceanic Waters: Accounting for Raman Emission and Varying Particle

Scattering Phase Function.” *Applied Optics* 41 (30): 6289–6306.
<https://doi.org/10.1364/AO.41.006289>.

“Roesler and Perry - 1995 - In Situ Phytoplankton Absorption, Fluorescence Emi.Pdf.” n.d.

Roesler, Collin S., and Mary Jane Perry. 1995. “In Situ Phytoplankton Absorption, Fluorescence Emission, and Particulate Backscattering Spectra Determined from Reflectance.” *Journal of Geophysical Research* 100 (C7): 13279.
<https://doi.org/10.1029/95JC00455>.

Stockley, Nicole D., Rüdiger Röttgers, David McKee, Ina Lefering, James M. Sullivan, and Michael S. Twardowski. 2017. “Assessing Uncertainties in Scattering Correction Algorithms for Reflective Tube Absorption Measurements Made with a WET Labs Ac-9.” *Optics Express* 25 (24): A1139. <https://doi.org/10.1364/OE.25.0A1139>.

Strait, Christopher, Michael Twardowski, Fraser Dalglish, Alberto Tonizzo, and Anni Vuorenkoski. 2018. “Development and Assessment of Lidar Modeling to Retrieve IOPs.” In *Ocean Sensing and Monitoring X*, edited by Weilin “Will” Hou and Robert A. Arnone, 10631:243 – 249. SPIE. <https://doi.org/10.1117/12.2309998>.

Twardowski, Michael S., Emmanuel Boss, Jacob B. Macdonald, W. Scott Pegau, Andrew H. Barnard, and J. Ronald V. Zaneveld. 2001. “A Model for Estimating Bulk Refractive Index from the Optical Backscattering Ratio and the Implications for Understanding Particle Composition in Case I and Case II Waters.” *Journal of Geophysical Research: Oceans* 106 (C7): 14129–42. <https://doi.org/10.1029/2000JC000404>.

Twardowski, Michael S., James M. Sullivan, Percy L. Donaghay, and J. Ronald V. Zaneveld. 1999. "Microscale Quantification of the Absorption by Dissolved and Particulate Material in Coastal Waters with an Ac-9." *Journal of Atmospheric and Oceanic Technology* 16 (6): 691–707. [https://doi.org/10.1175/1520-0426\(1999\)016<0691:MQOTAB>2.0.CO;2](https://doi.org/10.1175/1520-0426(1999)016<0691:MQOTAB>2.0.CO;2).

Vuorenkoski, Anni K., Fraser R. Dalgleish, Michael S. Twardowski, Bing Ouyang, and Charles C. Trees. 2015. "Semi-Empirical Inversion Technique for Retrieval of Quantitative Attenuation Profiles with Underwater Scanning Lidar Systems." In , edited by Weilin W. Hou and Robert A. Arnone, 94590E. <https://doi.org/10.1117/12.2180158>.

Walker, Ronald E., and John W. McLean. 1999. "Lidar Equations for Turbid Media with Pulse Stretching." *Applied Optics* 38 (12): 2384. <https://doi.org/10.1364/AO.38.002384>.

Zege, Eleonora, Iosif Katsev, and Alexander Prikhach. 2007. "Retrieval of Seawater Inherent Optical Properties Profiles from Lidar Waveforms." In , edited by Iosif M. Levin, Gary D. Gilbert, Vladimir I. Haltrin, and Charles C. Trees, 66150B-66150B – 9. <https://doi.org/10.1117/12.740450>.

Zege, Eleonora P, Iosif L Katsev, and Alexander S Prikhach. 2007. "INVERSION OF AIRBORNE OCEAN LIDAR WAVEFORMS," April, 5.

Zhang, Xiaodong, Lianbo Hu, and Ming-Xia He. 2009. "Scattering by Pure Seawater: Effect of Salinity." *Optics Express* 17 (7): 5698. <https://doi.org/10.1364/OE.17.005698>.

Zhou, Yudi, Weibiao Chen, Xiaoyu Cui, Aleksey Malinka, Qun Liu, Bing Han, Xueji Wang, et al. 2019. "Validation of the Analytical Model of Oceanic Lidar Returns: Comparisons with Monte Carlo Simulations and Experimental Results." *Remote Sensing* 11 (16): 1870. <https://doi.org/10.3390/rs11161870>.